1	Influence of Walker Circulations on East African Rainfall
2	
3	
4	
5	Siyu Zhao and Kerry H. Cook
6	
7	Department of Geological Sciences, University of Texas at Austin, Austin, TX, USA
8	
9	
10	
11	
12	Reference:
13	Zhao, S., Cook, K.H. (2021) Influence of Walker circulations on East African rainfall.
14	Climate Dynamics, <a href="https://doi.org/10.1007/s00382-020-05579-7">https://doi.org/10.1007/s00382-020-05579-7</a>
15	
16	
17	
18	

# Abstract

Walker circulations near East Africa are identified and their influence on the
interannual variability of East African rainfall is explored in multiple reanalyses and
observational precipitation datasets. The robustness of methodology for identifying 2-
dimensional overturning circulations in a three-dimensional flow is investigated. Three
Walker circulations with potential relevance to East African rainfall are identified,
namely, the East African, the Congo Basin, and the Indian Ocean Walker circulations.
Consistent anti-correlations across the reanalyses exist for the upward and
downward branches of the Indian Ocean Walker Circulation during September – March,
with strongest connections during October – December; they do not emerge for the other
two Walker circulations. Less (more) precipitation occurs over East Africa in the short-
rains season when the Indian Ocean Walker Circulation is anomalously strong (weak).
These rainfall variations are associated with anomalous mid-level moisture divergence
that primarily results from variations in wind divergence rather than atmospheric
moisture. The anomalous horizontal advection of moist static energy can be important in
modulating convection, but this argument is not conclusive considering the unclosed
budget and the variations within the composites. The associations above do not indicate
causality. Caution is advisable when using the concept of Walker circulations because a
two-dimensional streamfunction can over-simplify the complexity of the three-
dimensional circulation.

**Keywords:** East Africa; East African precipitation; East African short rains; Walker circulation; Indian Ocean Walker Circulation; Congo Basin Walker Circulation

### 1 Introduction

42

43

44

45

46

47

48

49

50

51

52

53

54

55

56

57

58

59

60

61

62

63

Most regions in East Africa have bimodal seasonal precipitation, with an overall arid or semi-arid climate (Ongoma and Chen 2017). Much of the precipitation is delivered during March-May and October-December, known as the long rains and the short rains seasons, respectively. For most of the year, the lower atmosphere over these bimodal regions is convectively-stable (Yang et al. 2015), and dominated by convergence near the surface, mid-level divergence, and upper-level convergence. Mid-level subsidence is present throughout the year, except during the long rains. Some studies relate these regional-scale circulation and precipitation features to larger-scale Walker circulations (Hastenrath 2000; Williams and Funk 2011; Liebmann et al. 2014, 2017). The purpose of this paper is to better understand the role of Walker circulations in influencing East African rainfall. Communities in East Africa are heavily dependent on rainfall for agriculture and water resources, which makes them vulnerable to climate variation and change (Cook and Vizy 2013). However, coupled general climate models do not accurately simulate East African climate, underestimating the long rains and overestimating the short rains (Yang et al. 2014; Tierney et al. 2015; Ummenhofer et al. 2018). This undermines confidence in projected precipitation changes with global warming, although the relationship between a model's ability to accurately represent the current climate and produce reliable projections is not simple (Rowell et al. 2016; Walker et al. 2019). An improved simulation of present and future rainfall over East Africa requires further investigation of the physical processes. Here we focus on the relationships between the Walker circulations and East African rainfall; the processes that drive the development and variation of the Walker circulations are outside the scope of this study.

Section 2 reviews the general concepts of Walker circulations, as well as previous work on Walker circulations near East Africa and their relationships with local rainfall.

Section 3 describes the datasets and the methodology used to identify and measure Walker circulations, regional moisture sources, and energetics. Results are presented in section 4, and section 5 includes a summary and conclusions.

## 2 Background

The term "Walker circulation" was first introduced by Bjerknes (1969) to describe the thermally-driven, zonal, overturning circulation over the equatorial Pacific Ocean. Later studies postulated that Walker circulations occur over other longitudes (Flohn and Fleer 1975; Newell 1979; Webster and Chang 1988; Holton and Hakim 2013; Lau and Yang 2015), such as in the Atlantic (Kidson 1975; Wang 2002a; Jiang et al. 2015).

There are various ways to quantify Walker circulations. Indirect indices can be based on sea level pressure (Vecchi and Soden 2007; L'Heureux et al. 2013; Kociuba and Power 2015), the mid-level CO<sub>2</sub> (Jiang et al. 2010, 2013, 2015), water vapor transport (Sohn and Park 2010) and coral records (Stevenson et al. 2014;). Direct measures of Walker circulations often involve surface wind (England et al. 2014), divergent wind (Krishnamurti 1971; Sasaki et al. 2014; He and Soden 2015) and the 500-hPa vertical p-velocity (Wang 2002b; Chung et al. 2019). Several methods have been developed to

isolate the effects of Walker circulations from Hadley or monsoon circulations (Tanaka et al. 2004; Gastineau et al. 2009; Yu and Zwiers 2010; Schwendike et al. 2014, 2015).

East Africa and the western Indian Ocean and its ascending branch over the Martime Continent. Some studies reported that it is present only during the boreal fall (Hastenrath 2000, 2007a; Hastenrath and Lamb 2004). However, other studies apply different metrics to measure Walker circulations and find different structure and seasonality. Pohl and Camberlin (2011) suggested the Indian Ocean Walker circulation exists throughout the year except the boreal summer, based on the anti-correlation between lower- and upper-level zonal winds over the equatorial central Indian Ocean. With the zonal streamfunction or the Ψ-vector method, the Indian Ocean Walker circulation was found stronger during the boreal summer and weaker during boreal winter (Yu et al. 2012; Schwendike et al. 2014). Schwendike et al. (2014) also showed the Indian Ocean Walker Circulation is centered over the west coast of Australia during the boreal winter.

The strength of the Indian Ocean Walker Circulation, often represented by the low-level zonal wind over the equatorial central Indian Ocean, has been linked to the East African short rains (Hastenrath et al. 1993; Hastenrath 2007b; Pohl and Camberlin 2011; Lyon 2014; Limbu and Guirong 2019). Similar connections have been identified with rainfall-related variables, such as lake levels (Bergonzini et al. 2004) and the  $\delta^{18}$ O composition of rainfall (Vuille et al. 2005). Accompanying an anomalous Walker Circulation are changes in vertical motion, low-level divergence and precipitable water amounts over East Africa and the western Indian Ocean, which favor anomalies of the East African short rains (Hastenrath and Polzin 2005).

The relationship between the Indian Ocean Walker Circulation and the East African long rains is not clear. First, there is no agreement about whether there is a Walker Circulation over the Indian Ocean during the boreal spring (Liebmann et al. 2014, 2017). In addition, the studies have not reached a consensus about the relationship with the East African long rains. On interannual time scales, Pohl and Camberlin (2011) showed a weak but significant correlation between the zonal wind (shear) over the Indian Ocean and the long rains, while Lyon (2014) found no statistically significant correlation. The Congo Basin Walker Circulation is also located near East Africa, with an upward branch over the Congo Basin and a downward branch over the eastern equatorial Atlantic Ocean. Seasonality of this Walker circulation is not fully consistent among the few available studies. Pokam et al. (2014) suggested that the Walker circulation is present throughout the year, strongest in June – August and weakest in March – May. Longandjo and Rouault (2020) proposed a similar seasonality. However, Cook and Vizy (2016) indicated that the Walker circulation only occurs during June – October when the Atlantic cold tongue has formed. There is agreement that this Walker circulation has minor influence on Congo Basin rainfall. While no relationship has been identified between the Congo Basin Walker Circulation and East African rainfall, the advection of moisture from the Congo Basin has been associated with East African rainfall (Nicholson, 1996; Diem et al. 2019). The purpose of this paper is to understand the influence of Walker circulations on East African rainfall. We identify Walker circulations near East Africa and investigate their relationships with monthly East African precipitation on interannual time scales. We

109

110

111

112

113

114

115

116

117

118

119

120

121

122

123

124

125

126

127

128

129

130

further focus on the link between the strength of the Indian Ocean Walker Circulation and East African rainfall and examine the underlying processes.

133

134

135

136

137

138

139

140

141

142

143

144

145

146

147

148

149

150

151

152

131

132

# 3 Methodology

Four reanalyses are examined to provide monthly estimates of atmospheric circulation variables. They are the 1.5°-resolution ERA-Interim Reanalysis (ERAI; Dee et al. 2011), the 1.25°-resolution Japanese Reanalysis (JRA-55; Kobayashi et al. 2015), the 0.625×0.5°-resolution (longitude-by-latitude) Modern-Era Retrospective analysis for Research and Applications, Version 2 (MERRA-2; Gelaro et al. 2017), and the 0.25°resolution ERA-5 reanalysis (Copernicus Climate Change Service, 2017). The analysis periods are 1979-2018 for ERAI, JRA55 and ERA5, and 1980-2018 for MERRA2. Four precipitation datasets are used, rather than relying on reanalysis rainfall rates. They are the 0.25°-resolution NOAA Precipitation Estimation from Remotely Sensed Information using an Artificial Neural Network Climate Data Record (PERSIANN; Ashouri et al. 2015), the 0.05°-resolution Climate Hazards Group InfraRed Precipitation with Station Data, Version 2 (CHIRPS2; Funk et al. 2015), the 0.25°resolution Tropical Rainfall Measurement Mission Multi-satellite Precipitation Analysis (TMPA; Huffman et al. 2007), and the 0.1°-resolution NOAA Climate Prediction Center African Rainfall Climatology Version 2.0 dataset (ARC2; Novella and Thiaw 2013). The records start in 1981 for CHIRPS2, 1983 for PERSIANN and ARC2, and 1998 for TMPA. CHIRPS2 provides precipitation estimates for land only, and ARC2 provides rainfall estimates over a limited area (20°W-55°E, 40°S-40°N).

Harmonic analysis is used to identify an analysis region that is relatively uniform in its precipitation seasonality over a large and contiguous area, following Yang et al. (2015) and Dunning et al. (2016). Using the discrete Fourier Transform, the time series of precipitation at each grid point is transformed into a same-length series in the frequency domain. Seasonality is categorized by comparing the amplitudes of the semiannual ( $c_2$ ) and annual ( $c_1$ ) harmonics in the transformed series. A region is categorized as bimodal when its semi-annual precipitation variance is larger than its annual variance (i.e.,  $log_2|c_2/c_1|>0$ ).

The  $\Psi$ -vector method developed by Keyser et al. (1989) and Schwendike et al. (2014) is used to visualize overturning zonal circulations. The vector stream function,  $\Psi = (\psi_x, \psi_y)$ , projects onto the zonal and meridional planes and provides an objective way of separating a three-dimensional circulation into two mass-conserved independent components. Accordingly, the vertical p-velocity  $(\omega)$  is decomposed into zonal and meridional components  $(\omega_x \text{ and } \omega_y)$ . To identify Walker circulations, only the zonal components  $(\psi_x \text{ and } \omega_x)$  are considered.

A solution for  $\psi_x$  can be found either by vertically integrating the divergent component of the zonal wind or by taking the gradient of the inverse Laplacian of the vertical p-velocity along a pressure surface (Hu et al. 2017). We find that these two solutions yield similar results. Here we present results for  $\psi_x$  calculated from the divergent component of the zonal wind,  $u_p$ , according to

$$\psi_x = -\int_0^p u_D \, dp \tag{1}$$

similar to the methodology used by Trenberth et al. (2000), Yu and Boer (2002), Bayr et al. (2014), and others. Then,  $\omega_x$  is defined as:

$$\omega_{\chi} = \frac{1}{a\cos\phi} \frac{\partial \psi_{\chi}}{\partial \lambda} \tag{2}$$

where a is the radius of the Earth (6371.2 km),  $\phi$  is latitude in radians, and  $\lambda$  is longitude.

A straightforward method to solve for  $u_D$  globally is by the Helmholtz decomposition. However, its application over a limited domain introduces a harmonic wind component that is induced by vorticity and divergence outside the domain (Adames et al. 2014; Cao et al. 2014). The harmonic wind component is irrotational and nondivergent, which leads to internal cancellation between  $\omega_x$  and  $\omega_y$  (Keyser et al. 1989).

To solve for  $u_D$  over a limited domain, Bishop (1996) and Adames et al. (2014) developed an attribution technique using free-space Green's functions. For a zonal channel from 10°S to 10°N,

186 
$$u_D(\lambda, \phi) = \frac{1}{4\pi a} \sum_{k=1}^{M-1} \sum_{l=1}^{N-1} F_{kl} \frac{\cos \phi'_{kl} \sin(\lambda - \lambda'_{kl})}{1 - \cos \gamma_{kl}}, \tag{3}$$

where the grid is indexed by  $1 \le k \le M-1$  in longitude ( $\lambda$ ) and  $1 \le l \le N-1$  latitude ( $\phi$ ).  $F_{kl}$ 

is the flux element centered at the midpoint  $(\lambda'_{kl}, \phi'_{kl})$  of the  $kl^{th}$  grid estimated (Bishop

190 1996) as

191 
$$F_{kl} = \frac{a\Delta \lambda \cos\phi}{2} \left( v_{k+1,l+1} + v_{k,l+1} - v_{k+1,l} - v_{kl} \right) + \frac{a\Delta\phi}{2} \left( u_{k+1,l+1} + u_{k+1,l} - u_{k,l+1} - u_{kl} \right), \tag{4}$$

where u and v are the zonal and meridional winds,  $\Delta\lambda$  and  $\Delta\phi$  denote longitude and latitude increments, and  $\gamma$  is the central angle between  $(\lambda, \phi)$  and  $(\lambda'_{kl}, \phi'_{kl})$ . The domain is selected to capture divergence near the equator and retain a buffer for inaccuracies near the lateral boundaries. By excluding the background flow induced by vorticity and divergence outside the tropics, this method is aimed at minimizing internal cancellation between  $\omega_x$  and  $\omega_y$ .

Because partitioning a three-dimensional circulation into zonal and meridional streamfunctions is inherently unphysical, we compare  $\psi_x$  values with  $u_D$  calculated by both the Helmholtz decomposition and by the limited-domain attribution technique. In addition, we interpret  $\psi_x$  in relation to the full wind field.

Several indices are calculated from the 500-hPa vertical p-velocity ( $\omega$ 500),  $u_D$  and  $\psi_x$  to measure the strength of the Walker circulations, following previous studies (e.g., Hastenrath 2000; Yu and Zwiers 2010; Cook and Vizy 2016). The seasonal cycle is removed from these fields by subtracting climatological means averaged from 1979 (1980 in MERRA2) to 2018, and linear trends are removed from the deseasoned time series. A "flywheel check" is used to understand the extent to which the Walker circulations identified by  $\psi_x$  can be envisioned as overturning modes characterized by anti-correlations between  $\omega$ 500 values in the vertical branches of the circulations. Table 1 summarizes the indices used, and Figure 1 shows the averaging regions for these indices.

The atmospheric column moisture budget (Lenters and Cook 1995; Seager and Henderson 2013) is used to investigate the moisture sources associated with East African precipitation anomalies. For the time mean, over which water vapor trends in the atmospheric column are negligible, this water mass conservation statement can be written as

$$P = ET + C + A + R \tag{5}$$

where P is precipitation, ET is evapotranspiration, C is the convergence term, A is the moisture advection term, and R is the residual that represents precipitation due to orographic uplift and transient eddies as well as numerical error. C and A are defined as

$$C = -\frac{1}{\rho_{w}g} \int_{100hPa}^{\rho_{s}} (q\nabla \cdot \vec{v}) dp, \qquad (6)$$

220 and

221 
$$A = -\frac{1}{\rho_w g} \int_{100hPa}^{p_s} (\vec{v} \cdot \nabla q) dp, \qquad (7)$$

- where  $\rho_w$  is the density of water,  $p_s$  is surface pressure, g is gravitational acceleration, q is
- specific humidity, and  $\vec{v}$  is the horizontal wind vector.
- The column-integrated moist static energy (MSE) budget (Hill et al. 2017) is
- 225 employed to examine anomalous energetics of convection anomalies. MSE is a
- combination of thermal, potential and latent energy, which can be denoted as

$$h = c_p T + gz + L_v q, \tag{8}$$

- where h is the MSE,  $c_p$  is the specific heat capacity of dry air at constant pressure (1004)
- 229 J·kg<sup>-1</sup>·K<sup>-1</sup>), T is temperature, z is geopotential height, and  $L_v$  is the latent heat of
- vaporization of water  $(2.5 \times 10^6 \text{ J} \cdot \text{kg}^{-1})$ .
- The time-mean column-integrated MSE budget can be expressed as

232 
$$\frac{\partial \left\langle \xi \right\rangle}{\partial t} \approx -\left\langle \omega \frac{\partial h}{\partial p} \right\rangle - \left\langle \vec{v} \cdot \nabla h \right\rangle + F_{net} + R^*, \tag{9}$$

- 233 where  $\xi$  is the sum of internal, potential and latent energy,  $F_{net}$  is the net energy input and
- 234  $R^*$  is the residual.  $\langle \rangle \equiv \frac{1}{g} \int_{100\text{hPa}}^{p_s} ()dp. \ \xi = c_v T + gz + L_v q$ , where  $c_v$  is the specific heat
- 235 capacity of dry air at constant volume (717 J·kg<sup>-1</sup>·K<sup>-1</sup>).  $F_{net} = L_v E + H + R_t R_s$ , where
- 236  $L_{\nu}E$  and H are turbulent latent and sensible heat fluxes, and  $R_{t}$  and  $R_{s}$  are net radiative
- fluxes at the top and bottom of atmosphere.

The column-integrated MSE budget is an approximation (Betts 1974; Hill and Ming 2016) and h is not a conserved variable (Neelin 2007; Romps 2015). In particular, the budget is not closed when using reanalysis values because of mass and energy imbalances due to data interpolation (Trenberth 1991) and the relatively coarse time resolution (Haimberger et al. 2001). Previous studies (Trenberth 1991; Hill et al. 2017) introduce procedures for correcting imbalances, but they require estimates of the column-integrated MSE flux divergence using spherical harmonics that are sensitive to truncation limits (Trenberth et al. 2001, 2002; Trenberth and Stepaniak 2003). Thus, we admit that the budget is not closed and focus on the understating gained by examining changes in the horizontal and vertical MSE advection ( $H_{adv}$  and  $V_{adv}$ ). These are calculated using second-order centered finite differencing at each pressure level and then vertically integrated.

### 4. Results

- a. Rainfall seasonality over East Africa: Selection of the analysis region
- Figure 2a displays  $log_2|c_2/c_1|$  from the harmonic analysis described in the Methodology section using TMPA precipitation for 1998-2018. Bimodal precipitation ( $log_2|c_2/c_1|>0$ ; red shading) regions include eastern Kenya, Somalia, and southeastern Ethiopia, and a zonal equatorial region extending from Guinea to Uganda. (See Fig. 1 in Dunning et al. 2016). Results are similar using the other three precipitation datasets. The bimodal area to the east of 35°E and from 3°S 3°N is our "equatorial averaging region" (stippled in Fig. 2a).
- Figure 2b shows the monthly precipitation climatology averaged over the equatorial averaging region in various datasets. Reanalyses are included to evaluate their performance

The datasets are generally in good agreement, with the two rainy seasons well represented. However, ARC2 produces rainfall rates that are about 0.5-1 mm/day lower than the other

in capturing rainfall seasonality, since we analyze circulation fields using these datasets.

However, ARC2 produces fainfair rates that are about 0.3-1 min/day lower than the other

datasets from April through November, and ERAI has rainfall rates during November-

December that are about 0.5 mm/day higher.

The bimodal area identified in Fig. 2 extends to 12°N, but rainfall seasonality across this large meridional extent (3°S – 12°N) varies. Fig. 2c presents the monthly precipitation climatology averaged over land points in the northern part of the bimodal area (from 3°N to 12 °N) shown in Fig. 2a. The long rains season here has a shoulder in May, unlike the equatorial averaging region, and the short rains season is shifted earlier. Peak rainfall rates for both rainy seasons are about 1 mm/day lower than those in the equatorial averaging region. When the relationships between overturning circulations and East African precipitation are examined below, the northern part of the bimodal region is evaluated separately from the equatorial averaging region.

## b. Identification of overturning zonal circulations near East Africa

Figure 3 shows cross sections of the monthly climatology of  $\psi_x$  (shading) along with vectors composed of  $u_D$  and  $\omega_x$  multiplied by -100; all values are from ERAI and averaged between 3°S and 3°N.  $u_D$  is solved by the Helmholtz decomposition.

Three overturning zonal circulations that are potentially relevant to East African rainfall occur in January (Fig. 3a). A clockwise zonal circulation appears over East Africa (25°E – 35°E) that extends from 200 to 600 hPa and tilts westward with height below 600 hPa. We refer to this circulation as the East Africa Walker Circulation. Its downward

branch is located over East Africa and the western Indian Ocean ( $40^{\circ}E - 60^{\circ}E$ ), and its upward branch is over the Congo Basin ( $10^{\circ}E - 30^{\circ}E$ ). To its west, there is a counterclockwise zonal circulation over  $170^{\circ}W - 25^{\circ}E$ , referred to as the Congo Basin Walker Circulation (Cook and Vizy, 2016). It is centered at 600 - 800 hPa and has its downward branch over the Atlantic Ocean ( $170^{\circ}W - 40^{\circ}E$ ).

Another counterclockwise zonal circulation is present over the Indian Ocean (40°E – 100°E) centered at 300 – 600 hPa. This Indian Ocean Walker Circulation has a downward branch over East Africa and the western Indian Ocean (40°E – 60°E), and an upward branch near 100°E.

The Indian Ocean Walker Circulation persists throughout the year (Figs. 3a – 3l). It is weakest in January and strongest in June – September. The East Africa Walker Circulation is present year-round except during June and July, and is strongest in February – April and September – November. The Congo Basin Walker Circulation exists throughout the year; it is weakest in May and strongest in August.

Using the other three reanalyses (JRA55, MERRA2 and ERA5; not shown) results in similar overturning zonal circulation systems, but their magnitudes and structures vary somewhat. In addition, MERRA2 has a clockwise zonal circulation in the upper troposphere over  $10 - 20^{\circ}\text{E}$  in March – May. All of the reanalyses produce discontinuities in the streamfunction field, but in different locations. Taking January as an example, ERAI has discontinuities over  $100 - 110^{\circ}\text{E}$  (Fig. 3a). Over these regions, the downward  $\omega_x$  and upward  $\omega_y$  values cancel, which is not physical. JRA55 has discontinuities in  $\psi_x$  over 70 – 80°E and 90 – 100°E, and MERRA2 and ERA5 have discontinuities over  $15 - 20^{\circ}\text{E}$  and  $90 - 100^{\circ}\text{E}$ .

To interpret  $\psi_x$ , and especially to understand its discontinuities, we compare it with the total wind field. Figure 4 shows a vertical cross section of January winds averaged over  $3^{\circ}S - 3^{\circ}N$  in ERAI as an example.  $\omega$  is upward from  $60^{\circ}E$  to  $120^{\circ}E$ , including the regions where  $\omega_x$  is downward and  $\psi_x$  is discontinuous in Fig. 3a. This deficiency is due to the nondivergent component included in  $u_D$ , as discussed in Section 3. Similar discontinuities are found in the other months, with internal cancellation between a downward  $\omega_x$  and an upward  $\omega_y$  over East Africa and the Western Indian Ocean ( $40^{\circ}E - 60^{\circ}E$ ).

The limited-domain attribution technique to solve for  $u_D$  is tested to see if it reduces the discontinuities. Figures 5a-5d show the results for four representative months, January, April, July, and October, respectively. The general patterns are similar to Fig. 3. Except in September – October (November),  $\psi_X$  is clockwise over  $100^{\circ}\text{E} - 120^{\circ}\text{E}$  ( $100^{\circ}\text{E} - 140^{\circ}\text{E}$ ) as exemplified by Fig. 5d. Differences in magnitude also occur. If the latitudinal extent of the equatorial channel is broadened in the attribution technique,  $\psi_X$  is more similar to the Helmholtz decomposition results. Since the choice of the equatorial domain in the attribution technique is arbitrary and the discontinuities remain, the Helmholtz decomposition methodology is selected for the following analysis. Caution is appropriate, however, because the internal cancellation between  $\omega_X$  and  $\omega_Y$  indicates that the overturning zonal and meridional circulations are not cleanly separated. The  $\Psi$ -vector method also has limitations in resolving interference from topography (Trenberth et al. 2000).

We now explore the extent to which these circulation systems can be envisioned as "flywheels" characterized by significant anti-correlations between the vertical velocity over equatorial East Africa and the remote upbranches of the three overturning zonal circulations. Figure 6 presents correlations between the 500-hPa vertical p-velocity

averaged over the equatorial averaging region ( $\omega$ 500EA) and the 500-hPa vertical p-velocity throughout much of the tropics in ERAI. Correlation coefficients with amplitudes exceeding the 95% confidence level are stippled. In January (Fig. 6a), there is significant anti-correlation between equatorial East Africa and the Maritime Continent (9°S – 9°N, 110-150°E) in ERAI. The other three reanalyses indicate similar, weak anti-correlations but the significant areas are more scattered (not shown). In February (Fig. 6b), weak and mostly insignificant anti-correlation persists over the Maritime Continent in ERAI, but JRA55 and ERA5 retain significant anti-correlations (6°S – 6°N, 140-170°E). MERRA2 shows almost no anti-correlation over the Maritime Continent. In March – September (Figs. 6c – 6i), no significant and consistent anti-correlations emerge. In October – December (Figs. 6j – 6l), there are significant anti-correlations in all four reanalyses, stronger than those in January – February. We conclude that  $\omega$ 500EA is anti-correlated with the upward branch of the Indian Ocean Walker Circulation in October – February.

The degree of anti-correlation between  $\omega 500EA$  and the Congo Basin is not consistent among the reanalyses. In January – June (Fig. 6a – 6f) and October – December (Fig. 6j – 6l), no significant anti-correlation appears over the Congo Basin in ERAI. However, significant anti-correlations with central equatorial Africa occur in the other reanalyses for a few months, namely, February for MERRA2, April for JRA55, and April but further north of the equator in MERRA2 and ERA5. In July – September (Fig. 6g – 6i), significant anti-correlations emerge over the Congo Basin in ERAI. However, ERA5 does not reproduce these significant anti-correlations, and MERRA2 only agrees for September. JRA55 shows significant anti-correlation in September, but at 3 – 9°N.

Since there is little agreement among the reanalyses, we cannot conclude that there is a robust correlation between ω500EA and the East African/Congo Basin Walker Circulation. To confirm, we correlate  $\omega 500 \text{CB}_i$  (Table 1) with  $\omega 500$  over the tropics. Figure 7 presents the correlations with  $\omega 500 \text{CB}_3$  (3°S – 3°N, 20 – 30°E) in June through September. In the other months (not shown), there are few cases of significant anticorrelations over East Africa. In ERAI, a significant anti-correlation appears over northern Tanzania and southeastern Kenya in June (Fig. 7a), which extends over Somalia in July (Fig. 7b). Significant anti-correlations persist over northern Tanzania and southeastern Kenya in August and September (Fig. 7c - 7d). MERRA2 also indicates significant anticorrelations over Tanzania in June – August (Fig. 7e – 7g), which extend over eastern Kenya and southern Somalia in September (Fig. 7h). In contrast, JRA55 (Fig. 7i - 7l) and ERA5 (Fig. 7m - 7p) do not produce significant anti-correlations over East Africa. Performing the correlation analysis with other ω500CB<sub>i</sub> indices or at different pressure levels (850 hPa, 700 hPa, or 300 hPa) produces no consistent or significant anti-correlations over equatorial East Africa (not shown). To confirm the anti-correlation between ω500EA and the upward branch of the

352

353

354

355

356

357

358

359

360

361

362

363

364

365

366

367

368

369

370

371

372

373

To confirm the anti-correlation between  $\omega 500EA$  and the upward branch of the Indian Ocean Walker Circulation in October – February (Figs. 6),  $\omega 500$  averaged over the Maritime Continent is correlated with  $\omega 500$  over the tropics. Multiple subareas are used for averaging (Fig. 1) to better locate the upward branch and to avoid mixing heterogeneous vertical motion over the Maritime Continent. These include subareas at the equator, where the Coriolis force is weak and the upward branch ideally should be located, and subareas off the equator.

October shows the strongest anti-correlations between the equatorial indices,  $\omega$ 500IO<sub>3j</sub> (Table 1), and equatorial East Africa/western Indian Ocean in the four reanalyses. Averaging over the subarea located at (3°S – 3°N, 100°S – 110°N) generates the strongest anti-correlations in JRA55 and MERRA2, and relatively strong anti-correlations in ERAI and ERA5 (Figs. 8a – 8d). In ERAI (Fig. 8a), significant anti-correlation occurs across the bimodal areas of East Africa and the western Indian Ocean from 3°S to 9°N. The other three reanalyses produce similar anti-correlations, although the locations and amplitudes vary somewhat. The significant anti-correlations over East Africa occur over 0 – 9°N, 3°S – 6°N, and 0 – 9°N in JRA55 (Fig. 8b), MERRA2 (Fig. 8c), and ERA5 (Fig. 8d).

Significant anti-correlations between the equatorial indices and equatorial East Africa and/or the equatorial western Indian Ocean in the four reanalyses also occur in September – March, but not exactly over the equatorial East Africa/western Indian Ocean region in December and March in MERRA2 and ERA5 (not shown). The significant anti-correlations are isolated over the equatorial western Indian Ocean in February in MERRA2 and ERA5. In April – August (not shown), there is no consistent and significant anti-correlation between the  $\omega 500 IO_{3j}$  indices and the equatorial East Africa/western Indian Ocean region among the four reanalyses.

Some of the off-equator Maritime Continent indices ( $\omega$ 500IO<sub>1-2j</sub>, 4-5j) produce stronger anti-correlations over the equatorial East Africa/western Indian Ocean region than the equatorial indices ( $\omega$ 500IO<sub>3j</sub>), but their presence and locations vary with the reanalyses. However, significant correlations are clustered around the southeastern Indian Ocean in November for all four reanalyses. As an example (Figs. 8e – 8h),  $\omega$ 500IO<sub>42</sub> generates significant anti-correlations over the East African bimodal areas and the western Indian

Ocean in all four reanalyses. ERAI and ERA5 indicate additional significant anti-correlations over Uganda and Tanzania. This is also the case for December (Figs. 8i – 8l), when such indices are grouped around the subarea (3 – 9°N, 110 – 120°E) in all four reanalyses. ω500IO<sub>23</sub> shows significant anti-correlations over the equatorial East Africa and the western Indian Ocean in the four reanalyses, but the anti-correlations are smaller in areal extent and magnitude compared to those in October – November. Significant anti-correlations also emerge over eastern Tanzania in JRA55, MERRA2 and ERA5, western Ethiopia in MERRA2, and Uganda in MERRA2 and ERA5.

We conclude that the Indian Ocean Walker Circulation passes the "flywheel check" in September – March with significant correlations between the upward and downward branches. However, the circulation is still far from an idealized Walker circulation. The upward branch of the Indian Ocean Walker Circulation is not always centered over the equator, and the divergent wind generally contains strong meridional components. Due to the close connection between mid-tropospheric vertical motion and precipitation, the overturning mode of variability over the Indian Ocean identified by the flywheel check implies relationships between East African rainfall and the strength of Indian Ocean Walker circulation on interannual time scales for the months of September – March. In the next section, this potential relationship is examined directly.

## c. Relating the Indian Ocean Walker Circulation to East African precipitation

Table 2a shows correlations between the mean precipitation over the equatorial averaging region (Fig. 2) in PERSIANN and various indices of the Indian Ocean Walker circulation ( $\psi_x$ IO,  $u_D$ 850 and  $u_D$ 150; Table 1) from ERAI in September – March. The other

three reanalyses (not shown) produce similar results. Significant correlations appear between equatorial East African rainfall and the circulation indices in October – February, but not in September and March. Note, however, that a correlation between a horizontal index and East African rainfall is not necessarily indicative of a connection to a zonal overturning circulation.

Table 2b presents correlations between equatorial East African rainfall and ω500IO<sub>ij</sub> for different reanalyses. The indices that generate the strongest anti-correlations over the equatorial East Africa/western Indian Ocean region in most reanalyses are selected. Although the selection is somewhat subjective, they represent clusters of significant correlation. Consistent and significant correlations are seen in October – February. Combined with Table 2a, we can conclude that less (more) rain falls over equatorial East Africa with a strong (weak) Indian Ocean Walker Circulation in these months. However, such a relationship is not seen in September and March. As discussed in Section 4b, the anti-correlation between the vertical branches of the Indian Ocean Walker Circulation is weaker during these two months when the downward branch of the circulation is mainly located over the western Indian Ocean. Correlations between the bimodal region north of 3°N (Fig. 2) and the indices produce similar results, even though the region has a somewhat different rainfall seasonality from equatorial East Africa.

Compositing is used to select years with an anomalously strong or weak Indian Ocean Walker Circulation in October – February. Years when  $\psi_x$ IO is greater than +0.5 SD are selected for the "strong" composite and years when  $\psi_x$ IO is less than -0.5 SD comprise the "weak" composite. These years are similar among the four reanalyses; Table 3 lists the years that are consistent in at least three out of the four reanalyses. Since the

sample sizes are not large, cross sections of  $\psi_x$ ,  $u_D$  and  $\omega$  anomalies averaged from 3°S – 3°N are inspected for each selected year to ensure that an anomalous overturning zonal circulation is present. Most selected years pass this test, but the longitudinal extents and centers of the anomalies vary. The years that fail this test are excluded (strikethrough in Table 3). To sharpen the composites, years when the anomalous circulation is not located over the Central Indian Ocean in two or more reanalyses are also removed (strikethrough in Table 3). Compositing based on  $u_D850$  and  $u_D150$  provides nearly the same selection of years. Although composites based on  $\omega 500 IO_{ij}$  (Table 2b) generate different years,  $\omega 500 IO_{ij}$  is 0.5 SD above or below the mean in at least one reanalysis for most (89.4%) of the selected years in Table 3.

Figure 9 shows precipitation anomalies for the strong and weak composites in October – February in the PERSIANN dataset; anomalies in the other three datasets, CHIRPS2, ARC2 and TMPA, are similar (not shown). In the strong composite precipitation is 0.5 - 2 mm/day lower over the Kenyan and Somalian coasts in October (Fig. 9a). The rainfall anomalies spread over equatorial East Africa and Tanzania in November (Fig. 9b), and are centered over Tanzania in December (Fig. 9c). The precipitation anomalies are similar to the anti-correlated areas in the "flywheel checks" (Fig. 8). In January – February (Figs. 9d – 9e), less rain falls over Ethiopia, South Sudan, Uganda and farther over the western Indian Ocean. However, there are no significant precipitation anomalies over the bimodal area, although Table 2 indicates significant correlations between the regional rainfall and the Indian Ocean Walker Circulation indices. This disagreement is related to the fact that rainfall rates are low during these months.

In the weak composite (Figs. 9f - 9j) precipitation anomalies are roughly opposite to those in the strong composite, although there are some differences. In October – November (Figs. 9f - 9g), precipitation anomalies over equatorial East Africa are up to 3 mm/day, and coherent precipitation anomalies do not occur over Tanzania and Mozambique. In January – February (Figs. 9i - 9j), the anomalies are insignificant.

The column moisture budget is used to examine the role of the Indian Ocean Walker Circulation in supplying moisture for East African rainfall and its anomalies. The ERA5 reanalysis, with the highest resolution, is selected for this analysis. Results are presented for November, when East African rainfall has its strongest association with the strength of Indian Ocean Walker Circulation, but the conclusions also apply to October and December.

Figures 10a – 10e present anomalies of the moisture budget terms (Section 3) for the strong composite. The ERA5 precipitation anomalies (Fig. 10a) are similar to those in PERSIANN (Fig. 9b). Evapotranspiration anomalies are small (Fig. 10b). The C term (Fig. 10c) decreases significantly over East Africa, and is the major contributor to the reduced precipitation. Anomalies of the A term (Fig. 10d) and the residual term (Fig. 10e) oppose the C decreases over the East African bimodal areas and Tanzania.

In the weak composite (Figs. 10f - 10j), evapotranspiration (Fig. 10g) over the bimodal area in East Africa is slightly increased but changes in the C term are again dominant. The other terms modify the rainfall anomalies but play less important roles.

Vertical profiles of the anomalous C term and its zonal and meridional components for the strong and weak composites averaged between 3°S and 3°N are shown in Fig. 11. Since anomalies in the C term can be related to both wind divergence and specific humidity anomalies, these variables are also assessed. The dashed lines in Fig. 11 mark a longitudinal

range  $(37^{\circ}E - 43^{\circ}E)$  that covers most of equatorial East Africa and avoids the highest topography  $(35^{\circ}E - 37^{\circ}E)$ .

The C term is anomalously small over 700 - 900 hPa and large near the surface over equatorial East Africa ( $37^{\circ}E - 43^{\circ}E$ ) in the strong composite (Fig. 11a). Over the ocean ( $43^{\circ}E - 55^{\circ}E$ ), the decrease occurs near the surface. Low values of the C term at 700 – 900 hPa are attributed to both zonal and meridional changes (Figs. 11b – 11c), while the larger C term near the surface is due to zonal anomalies alone.

Anomalous divergence (Fig. 11d) is the key contributor to the C term anomalies. In the strong composite, anomalous subsidence over equatorial East Africa enhances the divergence at 700 - 900 hPa. Near the surface, the anomalous easterly  $u_D$  flows from the western Indian Ocean onto the coastal topography, generating increased divergence over the ocean and insignificant convergence over the land.

A reduction of specific humidity (Fig. 11e) also contributes to the C term anomalies, but they play a less important role. Negative moisture anomalies are largest over the ocean at 700 – 900 hPa, but also occur over land in the mid-troposphere and near the surface. However, specific humidity anomalies are small over equatorial East Africa around 800 hPa, where the C term anomalies are largest.

Anomalies for the weak composite (Figs. 11f – 11j) are generally opposite to those for the strong composite, but greater in magnitude except in October and December when magnitudes are similar. December also features insignificant divergence anomalies near the surface over equatorial East Africa like Fig. 11d and Fig. 11i. Almost no divergence anomalies appear near the surface over equatorial East Africa in the composites for October.

The 800 hPa level is examined to understand how the spatial patterns of the moisture budget terms (Figure 12) are related to the circulation and moisture fields. Moisture convergence anomalies are close to the C term anomalies at this level, in agreement with Fig. 10, although magnitudes may be smaller and less statistically significant.

511

512

513

514

515

516

517

518

519

520

521

522

523

524

525

526

527

528

529

530

531

532

533

In the strong composite, moisture convergence (Fig. 12a) is lower over most of Somalia, Kenya and Tanzania, similar to the distribution of anomalies in Fig. 10c over land. This is associated with anomalous moisture fluxes flowing from East Africa to the Indian Ocean or Central Africa. Moisture anomalies (Fig. 12b) are small over East Africa. Along with Figs. 11d – 11e, this confirms the dominant role of the circulation in generating the moisture convergence anomalies. The anomalous divergence is related to divergent winds in all directions. The westerly anomalies over the coast are not connected to significant westerly anomalies over the central Indian Ocean  $(60^{\circ}E - 90^{\circ}E)$ , as they weaken near 55°E in the composite. In about half of the composited years (not shown), anomalous coastal westerlies are weak and even easterly over  $45^{\circ}E - 65^{\circ}E$ . In other years, anomalous westerlies are more continuous from the East African coast to the central and eastern Indian Ocean. We conclude that the anomalous divergence and subsidence over East Africa in the strong composite are not simply induced by mass conservation associated with the lower branch of the Indian Ocean Walker Circulation. The weak composite (Figs. 12c - 12d) is, in general, the opposite of the strong composite.

The column-integrated MSE budget reveals the energetic constraints on the divergent circulation over East Africa. 6-hourly data in ERAI is used to estimate the non-linear terms. Results are shown for November, but variations exist among the months of

the short-rains season. The results are less statistically significant due to variations within small composites.

Figures 13a – 13e show anomalies of the MSE budget terms (Section 3) for the strong composite. The time-averaged trend of column-integrated total energy (excluding the kinetic energy) exhibits negative anomalies over East Africa (Fig. 13a). MSE import by vertical advection (Fig. 13b) is greater over East Africa and partially balanced by anomalous MSE export by the horizontal advection (Fig. 13c). There are also negative anomalies of energetic forcing (Fig. 13d) but their magnitudes are smaller than the advection anomalies. The residual (Fig. 13e) is not small. It includes transient-eddy MSE advection and indicates that the MSE budget is not closed.

In the weak composite (Figs. 13f – 13j), no significant averaged differences (Fig. 13f) occur over East Africa but the primary balance is again between the advection terms. The net energetic forcing (Fig. 13i) is significantly larger over the western Indian Ocean in association with increased clouds and reduced outgoing longwave radiation. The opposite does not emerge in the strong composite because there is cancellation with the latent heat flux that is enhanced by higher surface wind speeds (not shown).

In October and December (not shown), the primary balance is still between the advection terms, or between the advection and residual terms over East Africa. Anomalies of the net energetic forcing are similar to those of November, which mostly occur over the ocean. Although October composites show opposite column anomalies of vertical MSE advection to those of November over equatorial East Africa, the vertical profiles of the anomalies are roughly similar to those of November. The anomalies change sign through vertical layers and cancel in the column integration.

Figure 14 illustrates the vertical profiles of the vertical MSE advection over the equatorial averaging region (Fig. 2) for the strong and weak composites. The vertical MSE advection anomalies are attributed to changes in the divergent circulation and atmospheric stability. Accordingly, the anomalous vertical MSE advection can be decomposed into dynamic, thermodynamic and covariance terms, i.e.  $\delta(\omega \partial_p h) = \delta(\omega) \partial_p h + \omega \delta(\partial_p h) + \delta(\omega) \delta(\partial_p h)$ . These terms are also shown in Fig. 14.

In the strong composite, there is anomalous MSE import at 100-600 hPa, export at 600-850 hPa, and import at 850-1000 hPa, which indicates that the convection is anomalously shallow (Fig. 14a). The shallower convection is attributed to stronger subsidence at upper levels and weaker ascent in the mid-troposphere (Fig. 14b) as well as changes in the vertical MSE gradient (Fig. 14c). The vertical MSE gradient anomalies are primarily due to reduced specific humidity in a deep layer from 1000-300 hPa (Fig. 14d). There are no indications of the adiabatic warming or downward heat advection that would be associated with enhanced subsidence and upper-level flow of an anomalous Indian Ocean Walker Circulation. Fig. 14e decomposes the vertical MSE advection anomalies. The dynamic term,  $\delta(\omega)\partial_p h$ , is dominant throughout the troposphere. The weak composite (Figs. 14f-14j) opposes the strong composite in general.

In October and December, profiles of the vertical advection anomalies are roughly similar to those of November, except for the near-surface layer and the strong composite in October. For the strong composite in October, shifting the western boundary of the averaging region to  $\sim 38^{\circ}$ E produces similar profiles to those of November.

Figures 13 and 14 show that the primary MSE balance is between the dynamic terms of anomalous vertical advection,  $\delta(\omega)\partial_p h$ , and anomalous horizontal advection.

Thus, the anomalous vertical flow,  $\delta\omega$ , is potentially induced by the horizontal MSE advection anomalies locally. This coincides with the presence of an anomalous Indian Ocean Walker Circulation, but no simultaneous remote influence is identified. Caution is appropriate, however, because the MSE budget is not closed and there are variations among the composited years.

Cross-sections of the anomalous horizontal MSE advection averaged over 3°S – 3°N are plotted in Figure 15. In the strong composite (Fig. 15a), there is anomalous MSE export by horizontal advection at 700 – 900 hPa over equatorial East Africa. Anomalous MSE import occurs around 600 hPa over the western Indian Ocean, and sporadically over the East African Highlands.

The anomalies are decomposed into dynamic, thermodynamic and covariance components using  $\delta(\vec{v} \cdot \nabla h) = \delta(\vec{v}) \cdot \nabla h + \vec{v} \cdot \delta(\nabla h) + \delta(\vec{v}) \cdot \delta(\nabla h)$ , similar to Fig. 14. Unlike Fig. 14, none of the components dominates the horizontal MSE advection anomalies, since they enhance or cancel out each other in different vertical layers (not shown). Fig. 15b illustrates the mechanism associated with the dynamic term, showing horizontal wind anomalies and the climatological MSE. Anomalous westerlies at 600 - 700 hPa advect high MSE air into East Africa, while anomalous easterlies at 800 - 900 hPa advect low MSE air. The thermodynamic term results from climatological horizontal winds advecting anomalous MSE (Fig. 15c). The MSE is significantly lower over the ocean primarily due to reduced specific humidity, and the climatological easterlies bring anomalously dry air into East Africa between 400 hPa and 900 hPa. The weak composite (Figs. 15d – 15f) generally opposes the strong composite.

There are some variations among the months of the short-rains season and the composited years. In October, the horizontal MSE advection anomalies are similar to those in November at 850 – 900 hPa over 37°E – 45°E, but are more organized at 500 – 700 hPa over 35°E – 55°E. In December, the anomalies are weaker but of the same sign as in November at 800 – 900 hPa over equatorial East Africa (40°E – 45°E). The strength and location of the decomposed terms also vary to some extent. For example, the weak composite in December does not have a positive dynamic term anomaly at 800 – 900 hPa over equatorial East Africa.

### **5 Conclusions**

Walker circulations near East Africa are identified and their relationships with East African rainfall are explored in multiple reanalyses and observational precipitation datasets. Processes associated with the interannual variability of East African rainfall are investigated for November, when the East African short rains and their covariability with the strength of the Indian Ocean Walker Circulation both peak. This study is motivated by the need to improve our basic understanding of the dynamics of East African rainy seasons, and a lack of consensus about the existence and role of Walker circulations near East Africa and their role in East African rainfall variations.

The  $\Psi$ -vector method is used to decompose the three-dimensional circulation into mass-conserving, independent, zonal and meridional components. The zonal components are used to identify Walker circulations. A solution for the streamfunction in the zonal and vertical plane,  $\psi_x$ , is found by vertically integrating the divergent component of the zonal wind,  $u_D$ . Because partitioning a three-dimensional circulation into zonal and meridional

streamfunctions is inherently unphysical, we compare  $\psi_x$  values with  $u_D$  calculated by both a Helmholtz decomposition and by a limited-domain attribution technique. In addition, we interpret  $\psi_x$  in relation to the full wind field.

Three Walker circulations with potential relevance to East Africa rainfall are identified. The East African Walker Circulation has a descending branch over East Africa, and an ascending branch over the Congo Basin. It persists throughout the year except during June and July, and is strongest in February – April and September – November. To its west, the Congo Basin Walker Circulation connects upward motion over the Congo Basin with downward motion over the equatorial eastern Atlantic. This circulation system appears year-round, and is weakest in May and strongest in August. The third zonal overturning circulation is the larger-scale Indian Ocean Walker Circulation, with descent over the western Indian Ocean and ascent over the Maritime Continent. It exists throughout the year, and it is weakest in January and strongest in June – September.

A "flywheel check" is used to understand the extent to which the upward and downward branches of the Walker circulations vary synchronously. For the East African and Congo Basin Walker circulations, consistent correlations across the four reanalyses do not emerge. The lack of agreement among the reanalyses may be related to the scarcity of upper-air observations over Central Africa. In contrast, there are consistent and significant anti-correlations between the 500-hPa vertical velocity over the Maritime Continent and over equatorial East Africa/western Indian Ocean in the four reanalyses during September – March. Correlations are strongest in October – December. Such contrast between the Indian Ocean Walker Circulation and the other two Walker

circulations that are mostly located over land may imply a key role for air-sea interactions in forcing the anti-correlations between the vertical branches of Walker circulations.

The seasonal cycle of the Walker circulation strength indicated by  $\psi_x$  is different from the seasonal cycle of the correlations between vertical velocities across the equatorial Indian Ocean basin. Multiple factors, including relatively strong meridional winds, the Tropical East Jet and the Indian Monsoon, potentially increase the overall anticlockwise mass movement but disturb the anti-correlation between the vertical branches of the Indian Ocean Walker Circulation. The factors that are involved in the complex, three-dimensional flow cannot be fully described by  $\psi_x$ . Additionally, as mass conservation is not ensured in the equatorial zonal panel, anti-correlation between vertical branches does not necessarily occur within these equatorial zonal circulations. This raises caution about simply understanding vertical motion by mass conservation with zonal winds. Stability and the MSE budget also constrain the local convection. Thus, it is advisable to examine the anomalous moisture and energy transport over the vertical branches when examining the influence of Walker circulations on regional precipitation.

In years with an anomalously strong (weak) Indian Ocean Walker Circulation, less (more) precipitation occurs over East Africa in October – December. Anomalous mid-level moisture divergence associated primarily with variations of wind divergence rather than specific humidity is important in generating these interannual rainfall variations during the short rains. At lower levels, moisture flux convergence (divergence) over the coastal topography accompanies a strong (weak) Indian Ocean Walker Circulation in November – December. Shallower (deeper) convection is associated with anomalous moist static energy export (import) by horizontal advection at mid- to lower-

troposphere. However, this energetic argument is not conclusive because the budget is not closed for the space and time scales considered and there are variations among the composited years and the months that comprise the short rains season.

The results of this study do not necessarily imply that there is a direct, remote influence of the Maritime Continent region on East African rainfall. One concern is that the conceptualization of Walker Circulations does not capture the complex, 3-dimensionality of the actual wind flow. Further, the strong and weak composites are not sufficiently precise due to the lack of a universal and accurate way to define and quantify the strength of Walker circulations. The Walker circulations also vary in other parameters such as boundaries and center locations. The sample sizes do not lend strong statistical confidence as well. Finally, the associations identified in this study do not necessarily indicate causality. For example, anomalies in the Indian Ocean Walker Circulation and East African rainfall might be mutual responses to variations in sea surface temperatures in the western Indian Ocean (Ummenhofer et al. 2009; Lyon 2014; Liu et al. 2020) or the Mascarene High (Manatsa et al. 2014; Vizy and Cook 2020; Peng et al. 2020).

Another caveat is that there are non-physical discontinuities in the zonal streamfunction. Decomposing the vertical velocity into components that satisfy mass continuity of the zonal and meridional streamfunctions is not always physical. It reflects the existence of harmonic components in the divergent wind and that mass conservation is not ensured in the equatorial zonal plane. This problem persists when the divergent winds are calculated globally using the Helmholtz decomposition or over an equatorial channel using free-space Green's functions, and with different methods of computing the zonal streamfunction.

694	
695	Acknowledgements
696	Support from NSF Award #1701520 is gratefully acknowledged. The HPC and
697	database resources needed for the analysis were supplied by the Texas Advanced
698	Computing Center (TACC) at The University of Texas at Austin. URL:
699	http://www.tacc.utexas.edu. The authors thank Dr. Edward K. Vizy for general support
700	and helpful discussions.
701	
702	References
703	Adames ÁF, Patoux J, Foster RC (2014) The contribution of extratropical waves to the
704	MJO wind field. J Atmos Sci 71:155-176. https://doi.org/10.1175/JAS-D-13-084.1
705	Ashouri H, Hsu K-L, Sorooshian S, et al (2015) PERSIANN-CDR: Daily Precipitation
706	Climate Data Record from Multisatellite Observations for Hydrological and Climate
707	Studies. Bull Am Meteorol Soc 96:69–83. https://doi.org/10.1175/BAMS-D-13-
708	<u>00068.1</u>
709	Bayr T, Dommenget D, Martin T, Power SB (2014) The eastward shift of the Walker
710	Circulation in response to global warming and its relationship to ENSO variability.
711	Clim Dyn 43:2747–2763. https://doi.org/10.1007/s00382-014-2091-y
712	Bergonzini L, Richard Y, Petit L, Camberlin P (2004) Zonal circulations over the Indian
713	and Pacific oceans and the level of Lakes Victoria and Tanganyika. Int J Climatol
714	24:1613–1624. https://doi.org/10.1002/joc.1089
715	Betts AK (1974) Further Comments on "A Comparison of the Equivalent Potential
716	Temperature and the Static Energy." J Atmos Sci 31:1713–1715.

717	https://doi.org/10.1175/1520-0469(1974)031<1713:FCOCOT>2.0.CO;2
718	Bishop CH (1996) Domain-independent attribution. Part II: Its value in the verification of
719	dynamical theories of frontal waves and frontogenesis. J. Atmos. Sci. 53:253-262
720	Bjerknes J (1969) Atmospheric Teleconnections From the Equatorial Pacific 1. Mon
721	Weather Rev 97:163–172. https://doi.org/10.1175/1520-
722	0493(1969)097<0163:atftep>2.3.co;2
723	Cao J, Ran L, Li N (2014) An application of the Helmholtz theorem in extracting the
724	externally induced deformation field from the total wind field in a limited domain.
725	Mon Weather Rev 142:2060–2066. https://doi.org/10.1175/MWR-D-13-00311.1
726	Chung ES, Timmermann A, Soden BJ, et al (2019) Reconciling opposing Walker
727	circulation trends in observations and model projections. Nat Clim Chang 9:405-
728	412. https://doi.org/10.1038/s41558-019-0446-4
729	Cook KH, Vizy EK (2013) Projected changes in east african rainy seasons. J Clim
730	26:5931-5948. https://doi.org/10.1175/JCLI-D-12-00455.1
731	Cook KH, Vizy EK (2016) The Congo Basin Walker circulation: dynamics and
732	connections to precipitation. Clim Dyn 47:697-717. https://doi.org/10.1007/s00382-
733	015-2864-y
734	Copernicus Climate Change Service (C3S) (2017) ERA5: Fifth generation of ECMWF
735	atmospheric reanalyses of the global climate . Copernicus Climate Change Service
736	Climate Data Store (CDS). <a href="https://cds.climate.copernicus.eu/cdsapp#!/home">https://cds.climate.copernicus.eu/cdsapp#!/home</a>
737	Dee DP, Uppala SM, Simmons AJ, et al (2011) The ERA-Interim reanalysis:
738	configuration and performance of the data assimilation system. Q J R Meteorol Soc
739	137:553–597. https://doi.org/10.1002/qj.828

740 Diem JE, Sung HS, Konecky BL, et al (2019) Rainfall Characteristics and Trends—and 741 the Role of Congo Westerlies—in the Western Uganda Transition Zone of 742 Equatorial Africa From 1983 to 2017. J Geophys Res Atmos 124:10712–10729. 743 https://doi.org/10.1029/2019JD031243 744 Dunning CM, Black ECL, Allan RP (2016) The onset and cessation of seasonal rainfall 745 over Africa. J Geophys Res Atmos 121:11,405-411,424. 746 https://doi.org/10.1002/2016JD025428 747 England MH, Mcgregor S, Spence P, et al (2014) Recent intensification of wind-driven 748 circulation in the Pacific and the ongoing warming hiatus. Nat Clim Chang 4:222-749 227. https://doi.org/10.1038/nclimate2106 750 Flohn H, Fleer H (1975) Climatic teleconnections with the equatorial pacific and the role 751 of ocean/atmosphere coupling. Atmosphere (Basel) 13:96–109. 752 https://doi.org/10.1080/00046973.1975.9648391 753 Funk C, Peterson P, Landsfeld M, et al (2015) The climate hazards infrared precipitation 754 with stations--a new environmental record for monitoring extremes. Sci data 755 2:150066. https://doi.org/10.1038/sdata.2015.66 756 Gastineau G, Li L, Le Treut H (2009) The Hadley and Walker circulation changes in 757 global warming conditions described by idealized atmospheric simulations. J Clim 758 22:3993-4013. https://doi.org/10.1175/2009JCLI2794.1 759 Gelaro R, McCarty W, Suárez MJ, et al (2017) The Modern-Era Retrospective Analysis 760 for Research and Applications, Version 2 (MERRA-2). J Clim 30:5419–5454. 761 https://doi.org/10.1175/JCLI-D-16-0758.1 762 Haimberger L, Ahrens B, Hamelbeck F, Hantel M (2001) Impact of time sampling on

763 atmospheric energy budget residuals. Meteorol Atmos Phys 77:167-184. 764 https://doi.org/10.1007/s007030170025 765 Hastenrath S (2000) Zonal circulations over the equatorial Indian Ocean. J Clim 766 13:2746–2756. https://doi.org/10.1175/1520-767 0442(2000)013<2746:ZCOTEI>2.0.CO;2 768 Hastenrath S (2007a) Equatorial zonal circulations: Historical perspectives. Dyn Atmos 769 Ocean 43:16–24. https://doi.org/https://doi.org/10.1016/j.dynatmoce.2006.04.001 770 Hastenrath S (2007b) Circulation mechanisms of climate anomalies in East Africa and 771 the equatorial Indian Ocean. Dyn Atmos Ocean 43:25–35. 772 https://doi.org/https://doi.org/10.1016/j.dynatmoce.2006.06.002 773 Hastenrath S, Lamb PJ (2004) Climate dynamics of atmosphere and ocean in the 774 equatorial zone: A synthesis. Int J Climatol 24:1601–1612. 775 https://doi.org/10.1002/joc.1086 776 Hastenrath S, Nicklis A, Greischar L (1993) Atmospheric-Hydrospheric Mechanisms of 777 Climate Anomalies in the Western Equatorial Indian Ocean. J Geophys Res 778 98:20,219-20,355 779 Hastenrath S, Polzin D (2005) Mechanisms of climate anomalies in the equatorial Indian 780 Ocean. J Geophys Res D Atmos 110:1–7. https://doi.org/10.1029/2004JD004981 781 He J, Soden BJ (2015) Anthropogenic weakening of the tropical circulation: The relative 782 roles of direct CO2 forcing and sea surface temperature change. J Clim 28:8728– 783 8742. https://doi.org/10.1175/JCLI-D-15-0205.1 784 Hill SA, Ming Y (2016) Energetic and hydrological responses of Hadley circulations and 785 the African Sahel to sea surface temperature perturbations. Dissertation, Princeton

786 University 787 Hill SA, Ming Y, Held IM, Zhao M (2017) A moist static energy budget-based analysis 788 of the Sahel rainfall response to uniform oceanic warming. J Clim 30:5637–5660. 789 https://doi.org/10.1175/JCLI-D-16-0785.1 790 Holton JR, Hakim GJ (2013) Chapter 11 - Tropical Dynamics. In: Holton JR, Hakim 791 GJBT-AI to DM (Fifth E (eds). Academic Press, Boston, pp 377–411 792 Hu S, Cheng J, Chou J (2017) Novel three-pattern decomposition of global atmospheric 793 circulation: generalization of traditional two-dimensional decomposition. Clim Dyn 794 49:3573–3586. https://doi.org/10.1007/s00382-017-3530-3 795 Huffman GJ, Bolvin DT, Nelkin EJ, et al (2007) The TRMM Multisatellite Precipitation 796 Analysis (TMPA): Quasi-Global, Multiyear, Combined-Sensor Precipitation 797 Estimates at Fine Scales. J Hydrometeorol 8:38–55. 798 https://doi.org/10.1175/JHM560.1 799 Jiang X, Chahine MT, Olsen ET, et al (2010) Interannual variability of mid-tropospheric 800 CO2 from Atmospheric Infrared Sounder. Geophys Res Lett 37:1–5. 801 https://doi.org/10.1029/2010GL042823 802 Jiang X, Olsen ET, Pagano TS, et al (2015) Modulation of midtropospheric CO2 by the 803 south Atlantic walker circulation. J Atmos Sci 72:2241–2247. 804 https://doi.org/10.1175/JAS-D-14-0340.1 805 Jiang X, Wang J, Olsen ET, et al (2013) Influence of EL Niño on midtropospheric CO2 806 from Atmospheric infrared sounder and model. J Atmos Sci 70:223–230. 807 https://doi.org/10.1175/JAS-D-11-0282.1

Keyser D, Schmidt BD, Duffy DG (1989) A Technique for Representing Three-

808

809 Dimensional Vertical Circulations in Baroclinic Disturbances. Mon Weather Rev 810 117:2463-2494. https://doi.org/10.1175/1520-811 0493(1989)117<2463:ATFRTD>2.0.CO;2 812 Kidson JW (1975) Tropical Eigenvector Analysis and the Southern Oscillation. Mon. 813 Weather Rev. 103:187–196 814 Kobayashi S, Ota Y, Harada Y, et al (2015) The JRA-55 Reanalysis: General 815 Specifications and Basic Characteristics. J Meteorol Soc Japan Ser II 93:5–48. 816 https://doi.org/10.2151/jmsj.2015-001 817 Kociuba G, Power SB (2015) Inability of CMIP5 models to simulate recent strengthening 818 of the walker circulation: Implications for projections. J Clim 28:20–35. 819 https://doi.org/10.1175/JCLI-D-13-00752.1 820 Krishnamurti TN (1971) Tropical East-West Circulations During the Northern Summer. 821 J. Atmos. Sci. 28:1342–1347 822 L'Heureux ML, Lee S, Lyon B (2013) Recent multidecadal strengthening of the Walker 823 circulation across the tropical Pacific. Nat Clim Chang 3:571–576. 824 https://doi.org/10.1038/nclimate1840 825 Lau KM, Yang S (2015) Tropical Meteorology & Climate: Walker Circulation, Second 826 Edi. Elsevier 827 Lenters JD, Cook KH (1995) Simulation and Diagnosis of the Regional Summertime 828 Precipitation Climatology of South America. J Clim 8:2988–3005 829 Liebmann B, Bladé I, Funk C, et al (2017) Climatology and interannual variability of 830 boreal spring wet season precipitation in the eastern horn of Africa and implications 831 for its recent decline. J Clim 30:3867–3886. https://doi.org/10.1175/JCLI-D-16832 0452.1 833 Liebmann B, Bladé I, Kiladis GN, et al (2012) Seasonality of African Precipitation from 834 1996 to 2009. J Clim 25:4304–4322. https://doi.org/10.1175/JCLI-D-11-00157.1 835 Liebmann B, Hoerling MP, Funk C, et al (2014) Understanding recent eastern Horn of 836 Africa rainfall variability and change. J Clim 27:8630–8645. 837 https://doi.org/10.1175/JCLI-D-13-00714.1 838 Limbu PTS, Guirong T (2019) Relationship between the October-December rainfall in 839 Tanzania and the Walker circulation cell over the Indian Ocean. Meteorol Zeitschrift 840 28:453–469. https://doi.org/10.1127/metz/2019/0939 841 Liu W, Cook K, Vizy E (2020) Influence of Indian Ocean SST regionality on the East 842 African short rains. Clim Dyn. https://doi.org/10.1007/s00382-020-05265-8 843 Longandjo G-NT, Rouault M (2020) On the Structure of the Regional-Scale Circulation 844 over Central Africa: Seasonal Evolution, Variability, and Mechanisms. J Clim 845 33:145–162. https://doi.org/10.1175/jcli-d-19-0176.1 846 Lyon B (2014) Seasonal drought in the Greater Horn of Africa and its recent increase 847 during the March-May long rains. J Clim 27:7953–7975. 848 https://doi.org/10.1175/JCLI-D-13-00459.1 849 Manatsa D, Morioka Y, Behera SK, et al (2014) Impact of Mascarene High variability on 850 the East African "short rains." Clim Dyn 42:1259–1274. 851 https://doi.org/10.1007/s00382-013-1848-z 852 Neelin JD (2007) Moist dynamics of tropical convection zones in monsoons, 853 teleconnections, and global warming. In: The Global Circulation of the Atmosphere. 854 Princeton University Press, pp 267–301

855 Newell RE (1979) Climate and the Ocean. Am Sci 67:405–416 856 Nicholson SE (1996) A review of climate dynamics and climate variability in eastern 857 Africa. In: The Limnology, Climatology and Paleoclimatology of the East African 858 Lakes (T.C. Johnson, & E.O. Odada, Eds.) (1st ed.). CRC Press, pp 25–56 859 Novella NS, Thiaw WM (2013) African Rainfall Climatology Version 2 for Famine 860 Early Warning Systems. J Appl Meteorol Climatol 52:588–606. 861 https://doi.org/10.1175/JAMC-D-11-0238.1 862 Ongoma V, Chen H (2017) Temporal and spatial variability of temperature and 863 precipitation over East Africa from 1951 to 2010. Meteorol Atmos Phys 129:131-864 144. https://doi.org/10.1007/s00703-016-0462-0 865 Peng X, Steinschneider S, Albertson J (2020) Investigating Long-Range Seasonal 866 Predictability of East African Short Rains: Influence of the Mascarene High on the 867 Indian Ocean Walker Cell. J Appl Meteorol Climatol. 868 https://doi.org/10.1175/JAMC-D-19-0109.1 869 Pohl B, Camberlin P (2011) Intraseasonal and interannual zonal circulations over the 870 Equatorial Indian Ocean. Theor Appl Climatol 104:175–191. 871 https://doi.org/10.1007/s00704-010-0336-1 872 Pokam WM, Bain CL, Chadwick RS, et al (2014) Identification of processes driving low-873 level westerlies in West Equatorial Africa. J Clim 27:4245–4262. 874 https://doi.org/10.1175/JCLI-D-13-00490.1 875 Romps DM (2015) MSE minus CAPE is the true conserved variable for an adiabatically 876 lifted parcel. J Atmos Sci 72:3639–3646. https://doi.org/10.1175/JAS-D-15-0054.1 877 Rowell DP, Senior CA, Vellinga M, Graham RJ (2016) Can climate projection

878	uncertainty be constrained over Africa using metrics of contemporary performance?
879	Clim Change 134:621–633. https://doi.org/10.1007/s10584-015-1554-4
880	Sasaki W, Doi T, Richards KJ, Masumoto Y (2014) The influence of ENSO on the
881	equatorial Atlantic precipitation through the Walker circulation in a CGCM. Clim
882	Dyn 44:191–202. https://doi.org/10.1007/s00382-014-2133-5
883	Schwendike J, Berry GJ, Reeder MJ, et al (2015) Trends in the local Hadley and local
884	Walker circulations. J Geophys Res 120:7599–7618.
885	https://doi.org/10.1002/2014JD022652
886	Schwendike J, Govekar P, Reeder MJ, et al (2014) Local partitioning of the overturning
887	circulation in the tropics and the connection to the Hadley and Walker circulations. J
888	Geophys Res 119:1322–1339. https://doi.org/10.1002/2013JD020742
889	Seager R, Henderson N (2013) Diagnostic Computation of Moisture Budgets in the ERA-
890	Interim Reanalysis with Reference to Analysis of CMIP-Archived Atmospheric
891	Model Data. J Clim 26:7876–7901. https://doi.org/10.1175/JCLI-D-13-00018.1
892	Sohn BJ, Park SC (2010) Strengthened tropical circulations in past three decades inferred
893	from water vapor transport. J Geophys Res Atmos 115:1-9.
894	https://doi.org/10.1029/2009JD013713
895	Stevenson S, Wong H, Fink D (2014) recent weakening of the Walker Circulation. 1–15.
896	https://doi.org/10.1002/2014PA002683.Received
897	Tanaka HL, Ishizaki N, Kitoh A (2004) Trend and interannual variability of Walker,
898	monsoon and Hadley circulations defined by velocity potential in the upper
899	troposphere. Tellus, Ser A Dyn Meteorol Oceanogr 56:250–269.
900	https://doi.org/10.1111/j.1600-0870.2004.00049.x

901 Tierney JE, Ummenhofer CC, DeMenocal PB (2015) Past and future rainfall in the Horn 902 of Africa. Sci Adv 1:1-9. https://doi.org/10.1126/sciadv.1500682 903 Trenberth KE (1991) Climate Diagnostics from Global Analyses: Conservation of Mass 904 in ECMWF Analyses. J Clim 4:707–722. https://doi.org/10.1175/1520-905 0442(1991)004<0707:CDFGAC>2.0.CO;2 906 Trenberth KE, Caron JM, Stepaniak DP (2001) The atmospheric energy budget and 907 implications for surface fluxes and ocean heat transports. Clim Dyn 17:259–276. 908 https://doi.org/10.1007/PL00007927 909 Trenberth KE, Solomon A (1993) Implications of global atmospheric spatial spectra for 910 processing and displaying data. J. Clim. 6:531–545 911 Trenberth KE, Stepaniak DP, Caron JM (2000) The global monsoon as seen through the 912 divergent atmospheric circulation. J Clim 13:3969–3993. 913 https://doi.org/10.1175/1520-0442(2000)013<3969:TGMAST>2.0.CO;2 914 Trenberth KE, Stepaniak DP, Caron JM (2002) Accuracy of atmospheric energy budgets 915 from analyses. J Clim 15:3343-3360. https://doi.org/10.1175/1520-916 0442(2002)015<3343:AOAEBF>2.0.CO;2 917 Ummenhofer CC, Gupta A Sen, England MH, Reason CJC (2009) Contributions of 918 Indian Ocean sea surface temperatures to enhanced East African rainfall. J Clim 919 22:993-1013. https://doi.org/10.1175/2008JCLI2493.1 920 Ummenhofer CC, Kulüke M, Tierney JE (2018) Extremes in East African hydroclimate 921 and links to Indo-Pacific variability on interannual to decadal timescales. Clim Dyn 922 50:2971–2991. https://doi.org/10.1007/s00382-017-3786-7 923 Vecchi GA, Soden BJ (2007) Global Warming and the Weakening of the Tropical

924	Circulation. J Clim 20:4316–4340. https://doi.org/10.1175/JCLI4258.1
925	Vizy EK, Cook KH (2020) Interannual variability of East African rainfall: role of
926	seasonal transitions of the low-level cross-equatorial flow. Clim Dyn.
927	https://doi.org/10.1007/s00382-020-05244-z
928	Vuille M, Werner M, Bradley RS, et al (2005) Stable isotopes in East African
929	precipitation record Indian Ocean zonal mode. Geophys Res Lett 32:1-5.
930	https://doi.org/10.1029/2005GL023876
931	Walker DP, Birch CE, Marsham JH, et al (2019) Skill of dynamical and GHACOF
932	consensus seasonal forecasts of East African rainfall. Clim Dyn 53:4911–4935.
933	https://doi.org/10.1007/s00382-019-04835-9
934	Wang C (2002a) Atlantic climate variability and its associated atmospheric circulation
935	cells. J Clim 15:1516–1536. https://doi.org/10.1175/1520-
936	0442(2002)015<1516:ACVAIA>2.0.CO;2
937	Wang C (2002b) Atmospheric circulation cells associated with the El Nino-Southern
938	Oscillation. J Clim 15:399-419. https://doi.org/10.1175/1520-
939	0442(2002)015<0399:ACCAWT>2.0.CO;2
940	Webster PJ, Hai-Ru Chang (1988) Equatorial energy accumulation and emanation
941	regions: impacts of a zonally varying basic state. J. Atmos. Sci. 45:803-829
942	Williams AP, Funk C (2011) A westward extension of the warm pool leads to a westward
943	extension of the Walker circulation, drying eastern Africa. Clim Dyn 37:2417-2435.
944	https://doi.org/10.1007/s00382-010-0984-y
945	Yang W, Seager R, Cane MA, Lyon B (2015) The annual cycle of East African
946	precipitation. J Clim 28:2385–2404. https://doi.org/10.1175/JCLI-D-14-00484.1

947	Yang W, Seager R, Cane MA, Lyon B (2014) The East African Long Rains in
948	Observations and Models. J Clim 27:7185–7202. https://doi.org/10.1175/JCLI-D-
949	13-00447.1
950	Yu B, Boer GJ (2002) The roles of radiation and dynamical processes in the El Niño-like
951	response to global warming. Clim Dyn 19:539-553. https://doi.org/10.1007/s00382-
952	002-0244-x
953	Yu B, Zwiers FW (2010) Changes in equatorial atmospheric zonal circulations in recent
954	decades. Geophys Res Lett 37:1-5. https://doi.org/10.1029/2009GL042071
955	Yu B, Zwiers FW, Boer GJ, Ting MF (2012) Structure and variances of equatorial zonal
956	circulation in a multimodel ensemble. Clim Dyn 39:2403-2419.
957	https://doi.org/10.1007/s00382-012-1372-6
958	
959	

## **Table 1.** Indices for the Walker circulations.

Indices	Description
ω500ΕΑ	ω500 averaged over the equatorial averaging region in East Africa (Fig. 2).
ω500CB <sub>j</sub>	$\omega$ 500 averaged over the j <sup>th</sup> subarea in the Congo Basin region (3°S – 3°N, 10 – 35°E; Fig. 1).
ω500ΙΟ <sub>ί</sub>	$\omega$ 500 averaged over the ij <sup>th</sup> subarea in the Maritime Continent region (15°S – 15°N and 90 – 150°E; Fig. 1).
u <sub>D</sub> 850	850-hPa (150-hPa) u <sub>D</sub> averaged over the equatorial central Indian Ocean
$(u_D 150)$	$(3^{\circ}S - 3^{\circ}N, 60 - 90^{\circ}E).$
$\psi_x$ IO	$\psi_{x}$ vertically averaged from 300 to 600 hPa and averaged over the equatorial central Indian Ocean (3°S – 3°N, 60 – 90°E).

Table 2. (a) Correlations between the mean precipitation (mm/day) over the equatorial
East Africa averaging region (Fig. 2) in PERSIANN and various indices of the Indian
Ocean Walker Circulation (ψ<sub>x</sub>IO, u<sub>D</sub>850 and u<sub>D</sub>150) from ERAI in September – March.
(b) Correlations between equatorial East African rainfall, as in (a), and ω500IO<sub>ij</sub>
evaluated for different reanalyses. Correlation coefficients exceeding 90% are in italics,
and exceeding 95% are bold.

(a)	$\psi_{x}$ IO	u <sub>D</sub> 850	u <sub>D</sub> 150
SEP	-0.100	-0.176	0.131
OCT	-0.733	-0.664	0.701
NOV	-0.792	-0.799	0.698
DEC	-0.636	-0.669	0.548
JAN	-0.539	-0.582	0.361
FEB	-0.509	-0.482	0.456
MAR	-0.151	-0.086	0.193

(b)	ω500IO <sub>ij</sub>	ERAI	JRA55	MERRA2	ERA5
SEP	ω500IO <sub>32</sub>	0.055	-0.045	0.001	0.000
OCT	ω500IO <sub>32</sub>	0.405	0.467	0.440	0.465
NOV	ω500IO <sub>42</sub>	0.582	0.625	0.568	0.605
DEC	ω500IO <sub>23</sub>	0.581	0.687	0.738	0.637
JAN	ω500IO <sub>33</sub>	0.242	0.358	0.406	0.527
FEB	ω500IO <sub>34</sub>	0.572	0.349	0.440	0.516
MAR	ω500IO <sub>34</sub>	0.214	0.076	0.063	0.117

**Table 3.** Years when  $\psi_x$  IO is greater than +0.5 SD ("strong") or less than -0.5 SD ("weak") in October – February in at least three of the four reanalyses. Years without an anomalous overturning zonal circulation over the Indian Ocean or when the anomalous circulation is not located over the Central Indian Ocean in two or more reanalyses are removed from the composites (strikethrough).

OCT		N	OV	DEC		DEC		JAN		FEB	
Weak	Strong	Weak	Strong	Weak	Strong	Weak	Strong	Weak	Strong		
11	11	6	8	10	12	8	8	6	5		
1982	1981	1982	1979	<del>1979</del>	<del>1980</del>	1979	1984	<del>1980</del>	1984		
1987	1983	1984	1981	1985	1984	1983	<del>1986</del>	<del>1982</del>	1985		
1994	<del>1989</del>	1994	<del>1987</del>	1986	1987	1985	<del>1987</del>	1986	<del>1992</del>		
1997	1992	1997	1988	1988	1993	1992	<del>1989</del>	1987	<del>1994</del>		
2002	1996	2004	1995	1989	1996	<del>1996</del>	1990	1990	<del>1997</del>		
2004	1998	2006	1998	1990	1998	1998	<del>1991</del>	<del>1993</del>	2000		
2006	1999	<del>2011</del>	2001	1994	1999	2004	<del>1995</del>	1998	<del>2001</del>		
2009	2000		2005	<del>1995</del>	2005	<del>2007</del>	<del>1999</del>	<del>2006</del>	<del>2004</del>		
2011	2001		2010	1997	2007	2008	2000	<del>2010</del>	<del>2008</del>		
2012	<del>2005</del>			2001	2010	<del>2009</del>	2001	2014	2011		
2015	2010			<del>2002</del>	<del>2011</del>	2014	2011	<del>2017</del>	2013		
	2016			2004	2012		2012	2018			
	2017			2006	<del>2013</del>		2017				
					2014		2018				
					2016						

## **Figure Captions**

**Fig. 1** Averaging areas and subareas. The Congo Basin subareas to derive ω500CBj are marked by black boxes (3°S – 3°N and 10 – 35°E; j = 1, 2, 3, 4), and those used to derive ω500IOij are denoted by gray lines (15°S – 15°N and 90 – 150°E; i ranges from 1 to 5 and j ranges from 1 to 6). The averaging region for ω500EA over equatorial East Africa is denoted by the gray shading. The region is plotted on the horizontal grid of the TMPA data, but interpolated to the reanalysis grids for the "flywheel check". The averaging region for  $u_D850$ ,  $u_D150$ , and  $\psi_x$ IO in the central Indian Ocean is also shown (black square; 3°S – 3°N and 60 – 90°E).

**Fig. 2** (a) log<sub>2</sub>|c<sub>2</sub>/c<sub>1</sub>| from the harmonic analysis using TMPA precipitation over the 1998-2018 period. Contours denote surface geopotential height (m) over Africa in ERAI. The equatorial averaging region is stippled. (b) The monthly precipitation climatology averaged over the equatorial averaging region in observations and reanalyses. (c) The monthly precipitation climatology averaged over the northern part of the bimodal area (north of 3°N) in observations and reanalyses.

Fig. 3 Cross sections of the monthly climatology of  $\psi_x$  (shading; m·Pa·s<sup>-1</sup>),  $u_D$  (vectors; m·s<sup>-1</sup>) and  $\omega_x$  (vectors; Pa·s<sup>-1</sup>) averaged between 3°S and 3°N in ERAI.  $u_D$  is calculated with the Helmholtz decomposition on the global grid. Only one in two wind vectors are plotted for clarity. Green shading represents topography, constructed from the

1002 from 40°E to 47°E. 1003 Fig. 4 Wind vectors composed of the full zonal wind (m·s<sup>-1</sup>) and the vertical p-velocity 1004 1005 (Pa·s<sup>-1</sup>) averaged between 3°S and 3°N in ERAI. Only one in two wind vectors are plotted 1006 for clarity. The green shading represents topography, constructed from the climatological 1007 surface pressure in ERAI. 1008 Fig. 5 Cross sections of the monthly climatology of  $\psi_x$  (shading; m·Pa·s<sup>-1</sup>),  $u_D$  (vectors; 1009 m·s<sup>-1</sup>) and  $\omega_x$  (vectors; Pa·s<sup>-1</sup>) averaged between 3°S and 3°N in ERAI in (a) January, (b) 1010 1011 April, (c) July and (d) October.  $u_D$  is calculated using the limited-domain attribution 1012 technique. Only one in two wind vectors are plotted for clarity. Green shading represents 1013 topography, constructed from climatological surface pressure (hPa) in ERAI. 1014 Fig. 6 Monthly correlation between EAω500 and ω500 in ERAI. Correlation coefficients 1015 1016 exceeding the 95% confidence level are stippled, based on a two-tailed Student's t-test 1017 assuming 38 degrees of freedom. 1018 Fig. 7 Correlations between  $\omega 500$  averaged over the Congo Basin (3°S – 3°N, 20 – 30°E) 1019 1020 and  $\omega$ 500 in ERAI in (a) June, (b) July, (c) August, and (d) September. (e) – (h), (i) – (l) 1021 and (m) - (p) are the same as (a) - (d), but for MERRA2, JRA55 and ERA5, respectively. 1022 Correlation coefficients exceeding the 95% confidence level are stippled, based on a two-

climatological surface pressure (hPa) in ERAI. The coast of equatorial East Africa ranges

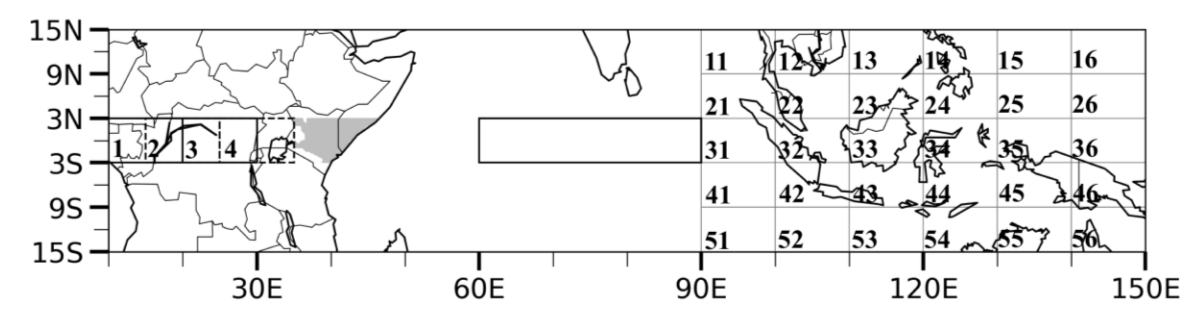
1023 tailed Student's t-test assuming 38 degrees of freedom (37 degrees of freedom for 1024 MERRA2). 1025 1026 Fig. 8 Correlations between  $\omega 500IO_{32}$  (green boxes;  $3^{\circ}S - 3^{\circ}N$ ,  $100 - 110^{\circ}E$ ) and  $\omega 500$ 1027 in October for (a) ERAI, (b) JRA55, (c) MERRA2 and (d) ERA5. Correlations between 1028  $\omega$ 500IO<sub>42</sub> (green boxes; 3°S – 9°S, 100 – 110°E) and  $\omega$ 500 in November for (e) ERAI, 1029 (f) JRA55, (g) MERRA2 and (h) ERA5. Correlations between ω500IO<sub>23</sub> (green boxes; 1030  $3^{\circ}N - 9^{\circ}N$ ,  $110 - 120^{\circ}E$ ) in December for (i) ERAI, (j) JRA55, (k) MERRA2 and (l) 1031 ERA5. Correlation coefficients exceeding the 95% confidence level based on a two-tailed 1032 Student's t-test assuming 38 degrees of freedom (37 degrees of freedom for MERRA2) 1033 are stippled. 1034 Fig. 9 Precipitation anomalies (mm·day<sup>-1</sup>) for the strong and weak composites in October 1035 1036 - February in PERSIANN. Values exceeding 95% confidence levels are stippled, based 1037 on a Welch's t-test. 1038 Fig. 10 Anomalies of moisture budget terms (mm·day<sup>-1</sup>) for the strong composite in 1039 1040 November calculated from ERA5: (a) P; (b) ET; (c) the C term; (d) the A term; and (e) 1041 the residual. (f) - (j) are anomalies of the moisture budget terms for the weak composite. 1042 Values exceeding the 95% confidence levels are stippled, based on a Welch's t-test. 1043 Fig. 11 Cross sections of the anomalous (a) C term (C; 10<sup>-8</sup>·s<sup>-1</sup>), (b) zonal component (Cz; 1044  $10^{-8} \cdot \text{s}^{-1}$ ), (c) meridional component (Cm;  $10^{-8} \cdot \text{s}^{-1}$ ), (d) divergence (DIV;  $10^{-6} \cdot \text{s}^{-1}$ ),  $\omega$ 1045

(vectors; Pa·s<sup>-1</sup>) and  $u_D$  (vectors; m·s<sup>-1</sup>), and (e) specific humidity (q;  $10^{-3} \cdot \text{kg} \cdot \text{kg}^{-1}$ ) for the strong composite in November in ERA5, averaged between 3°S and 3°N. (f) – (j) are anomalies for the weak composite. For clarity, vectors exceeding the 95% confidence levels are plotted every 1.5° longitude and every other pressure level. Values exceeding the 95% confidence levels are stippled, based on a Welch's t-test. The dashed lines mark  $37^{\circ}\text{E}$  and  $43^{\circ}\text{E}$ . The green block represents the topography, constructed from climatological surface pressure (hPa) in ERA5.

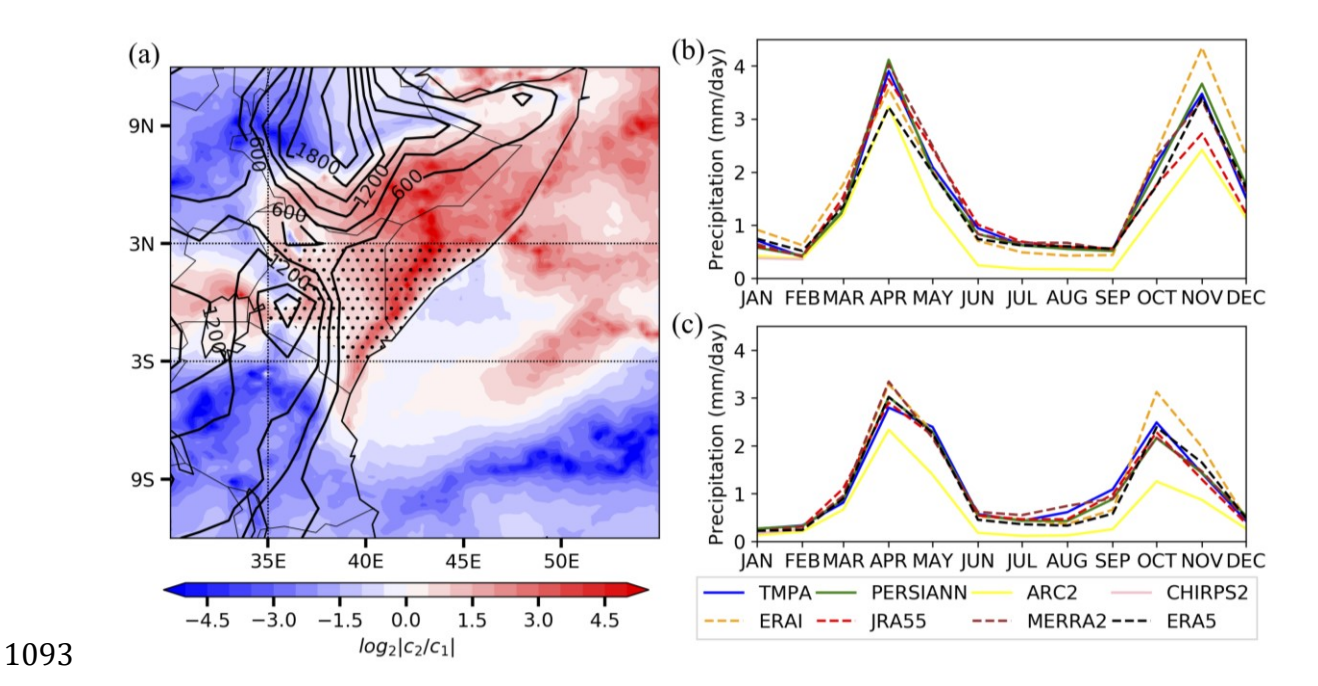
**Fig. 12** Anomalous (a) moisture convergence (shading;  $10^{-8} \cdot s^{-1}$ ) and moisture flux (vectors;  $m \cdot s^{-1}$ ), and (b) specific humidity (shading;  $10^{-3} \cdot kg \cdot kg^{-1}$ ) and divergent wind (vectors;  $m \cdot s^{-1}$ ) at 800 hPa for the strong composite in November in ERA5. (c) – (d) are anomalies for the weak composite. Vectors are plotted every 1.5° longitude/latitude for clarity, and marked green if exceeding 95% confidence levels. Values exceeding 95% confidence levels are stippled, based on a Welch's t-test.

Fig. 13 Anomalies of column-integrated MSE budget terms (W·m<sup>-2</sup>) for the strong composite in November calculated from 6-hourly data in ERAI: (a) the trend (b)  $V_{adv}$ , (c)  $H_{adv}$ , (d)  $F_{net}$ , and (e) the residual. (f) – (j) are anomalies of column-integrated MSE budget terms for the weak composite. Values exceeding the 95% confidence levels are stippled, based on a Welch's t-test.

**Figure 14.** Vertical profiles of (a)  $V_{adv}$  (10<sup>-3</sup>·W·kg<sup>-1</sup>), (b)  $\omega$  (10<sup>-2</sup>·Pa·s<sup>-1</sup>), (c) MSE 1067  $(10^5 \cdot \text{J} \cdot \text{kg}^{-1})$ , (d) anomalous MSE terms  $(10^3 \cdot \text{J} \cdot \text{kg}^{-1})$  and (e) anomalous  $V_{adv}$  terms  $(10^5 \cdot \text{J} \cdot \text{kg}^{-1})$ 1068 <sup>3</sup>·W·kg<sup>-1</sup>) for the strong composite (red lines) in November over the equatorial East 1069 1070 Africa averaging region (Fig. 2), calculated from ERAI. (f) – (j) are diagnostics for the 1071 weak composite (blue lines). Black lines in (a) – (c) and (f) – (h) denote vertical profiles 1072 for the climatology. 1073 **Figure 15.** Cross sections of (a) the anomalous  $H_{adv}$  (10<sup>-3</sup>·W·kg<sup>-1</sup>), (b) the climatological 1074 MSE (10<sup>5</sup>·J·kg<sup>-1</sup>) and the anomalous zonal wind (m·s<sup>-1</sup>) and vertical p-velocity (Pa·s<sup>-1</sup>) 1075 and (c) the anomalous MSE  $(10^3 \cdot J \cdot kg^{-1})$  and the climatological zonal wind  $(m \cdot s^{-1})$  and 1076 vertical p-velocity (Pa·s<sup>-1</sup>) for the strong composite in November calculated from ERAI. 1077 1078 (d) – (f) are diagnostics for the weak composite. Vectors are plotted every other longitude 1079 and pressure level for clarity. The green block represents the topography, constructed 1080 from climatological surface pressure (hPa) in ERAI.



1083 Figure 1. Averaging areas and subareas. The Congo Basin subareas to derive ω500CB<sub>i</sub> 1084 are marked by black boxes  $(3^{\circ}S - 3^{\circ}N)$  and  $10 - 35^{\circ}E$ ; j = 1, 2, 3, 4, and those used to 1085 derive ω500IO<sub>ii</sub> are denoted by gray lines (15°S – 15°N and 90 – 150°E; i ranges from 1 1086 to 5 and j ranges from 1 to 6). The averaging region for ω500EA over equatorial East Africa is denoted by the gray shading. The region is plotted on the horizontal grid of the 1087 TMPA data, but interpolated to the reanalysis grids for the "flywheel check". The 1088 1089 averaging region for  $u_D 850$ ,  $u_D 150$ , and  $\psi_x IO$  in the central Indian Ocean is also shown (black square;  $3^{\circ}S - 3^{\circ}N$  and  $60 - 90^{\circ}E$ ). 1090 1091



**Figure 2.** (a)  $\log_2|c_2/c_1|$  from the harmonic analysis using TMPA precipitation over the 1998-2018 period. Contours denote surface geopotential height (m) over Africa in ERAI. The equatorial averaging region is stippled. (b) The monthly precipitation climatology averaged over the equatorial averaging region in observations and reanalyses. (c) The monthly precipitation climatology averaged over the northern part of the bimodal area (north of 3°N) in observations and reanalyses.

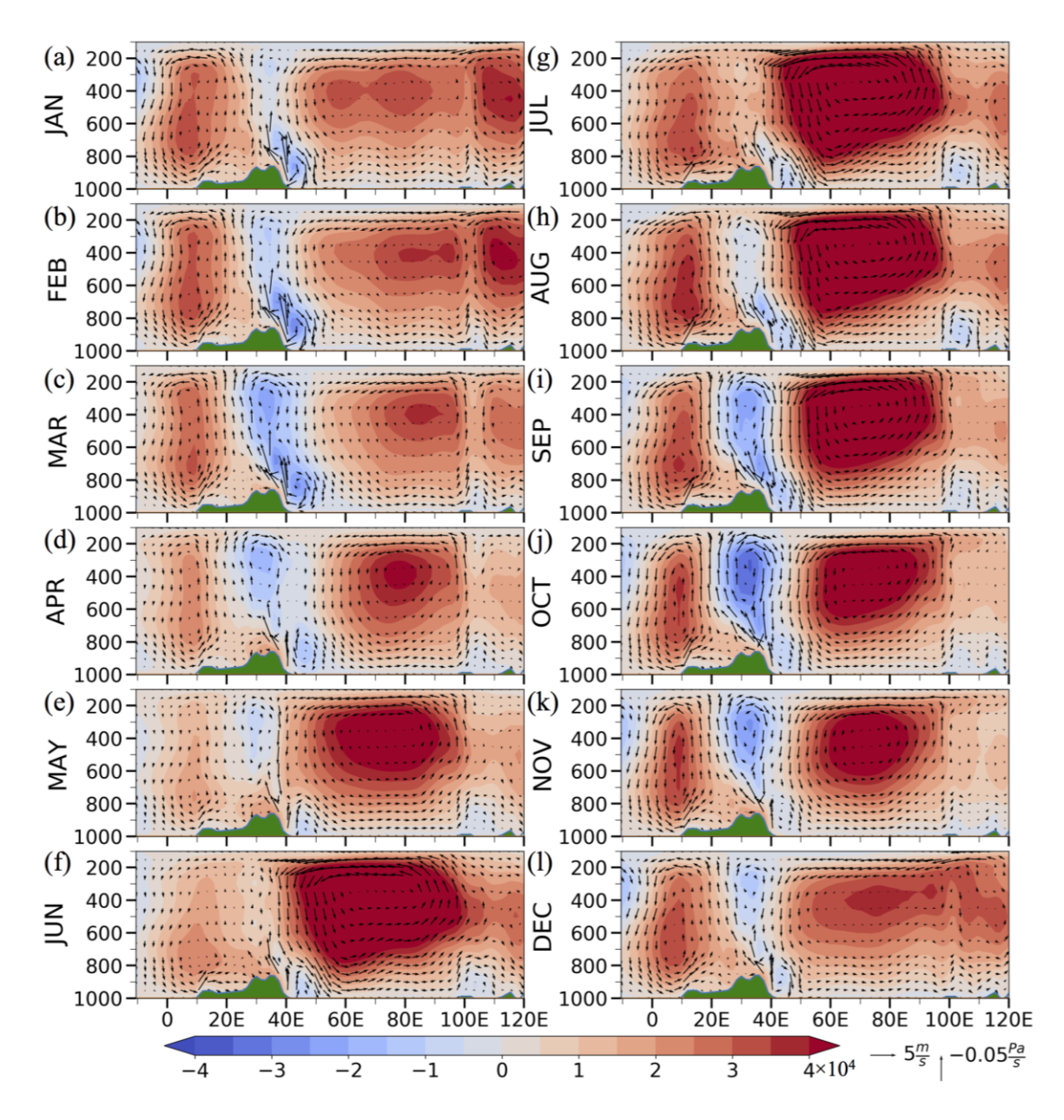


**Figure 3.** Cross sections of the monthly climatology of  $\psi_x$  (shading; m·Pa·s<sup>-1</sup>),  $u_D$  (vectors; m·s<sup>-1</sup>) and  $\omega_x$  (vectors; Pa·s<sup>-1</sup>) averaged between 3°S and 3°N in ERAI.  $u_D$  is calculated with the Helmholtz decomposition on the global grid. Only one in two wind vectors are plotted for clarity. Green shading represents topography, constructed from the climatological surface pressure (hPa) in ERAI. The coast of equatorial East Africa ranges from 40°E to 47°E.

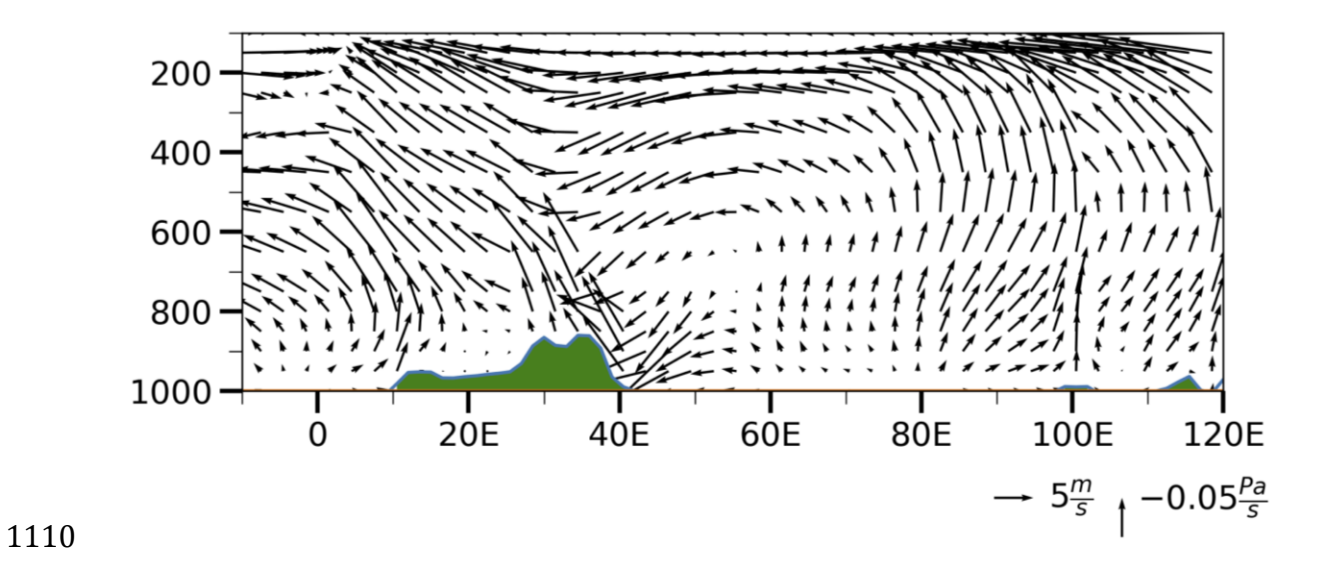


**Figure 4.** Wind vectors composed of the full zonal wind  $(m \cdot s^{-1})$  and the vertical p-velocity  $(Pa \cdot s^{-1})$  averaged between 3°S and 3°N in ERAI in January. Only one in two wind vectors are plotted for clarity. The green shading represents topography, constructed from the climatological surface pressure in ERAI.

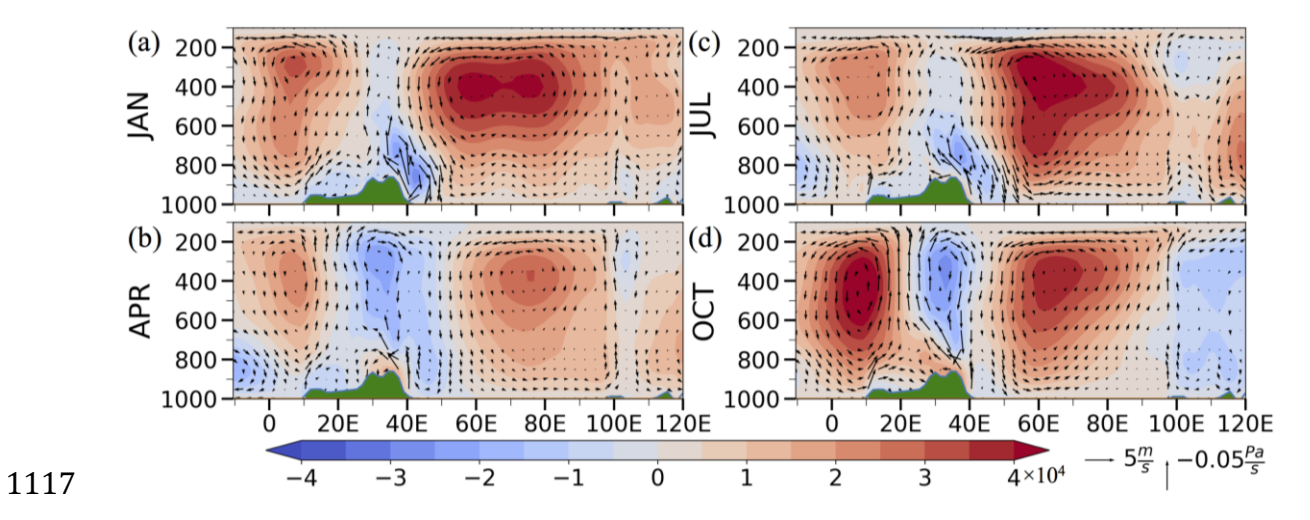


**Figure 5.** Cross sections of the monthly climatology of  $\psi_x$  (shading; m·Pa·s<sup>-1</sup>),  $u_D$  (vectors; m·s<sup>-1</sup>) and  $\omega_x$  (vectors; Pa·s<sup>-1</sup>) averaged between 3°S and 3°N in ERAI in (a) January, (b) April, (c) July and (d) October.  $u_D$  is calculated using the limited-domain attribution technique. Only one in two wind vectors are plotted for clarity. Green shading represents topography, constructed from climatological surface pressure (hPa) in ERAI.

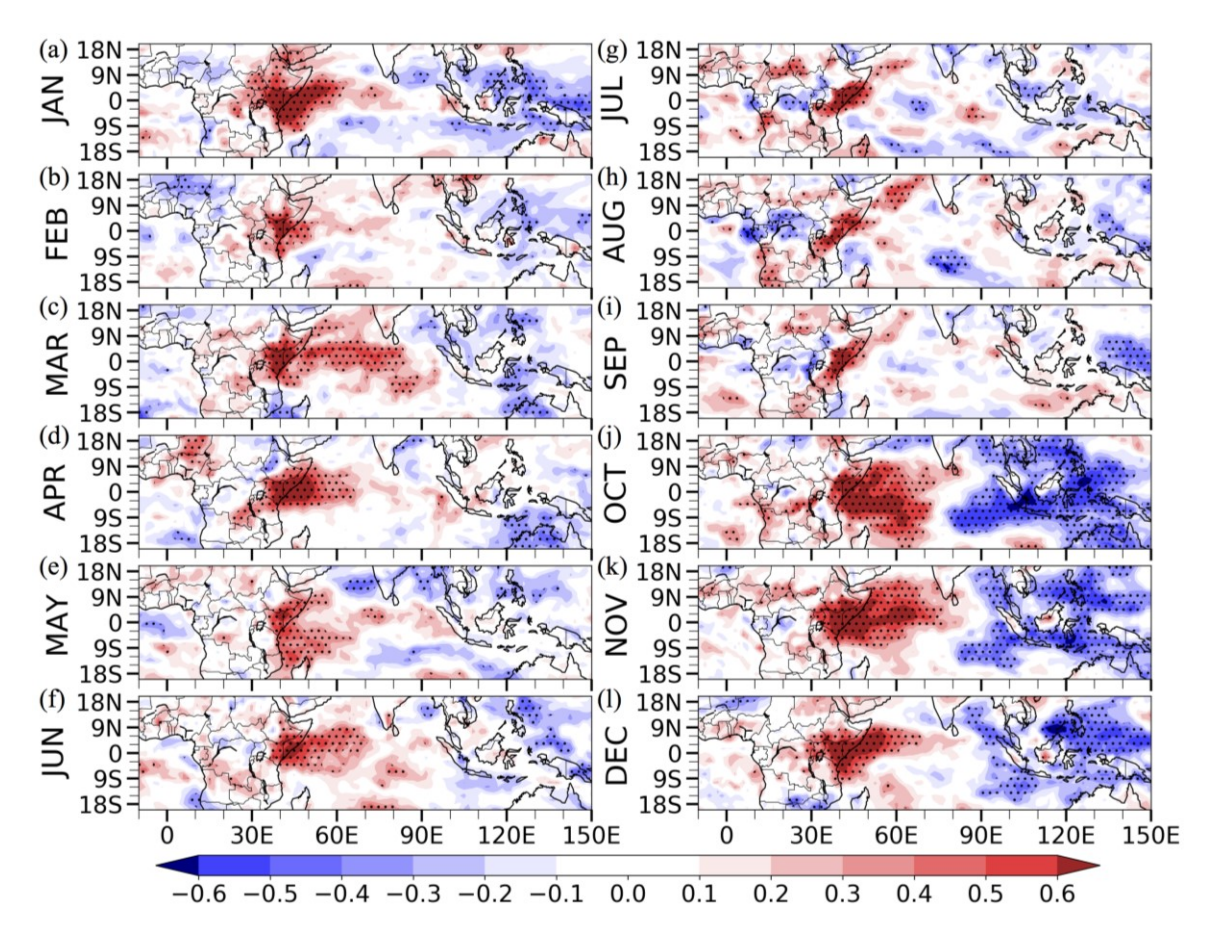


**Figure 6.** Monthly correlation between EA $\omega$ 500 and  $\omega$ 500 in ERAI. Correlation coefficients exceeding the 95% confidence level are stippled, based on a two-tailed Student's t-test assuming 38 degrees of freedom.

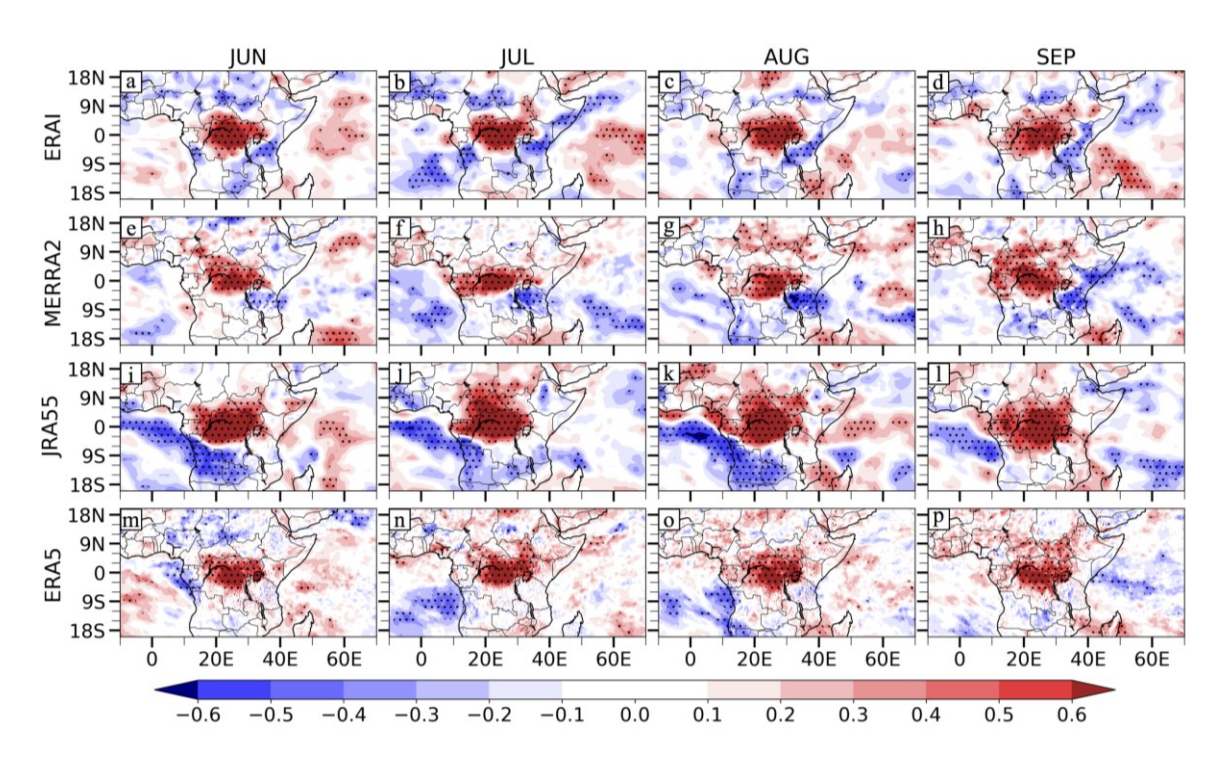
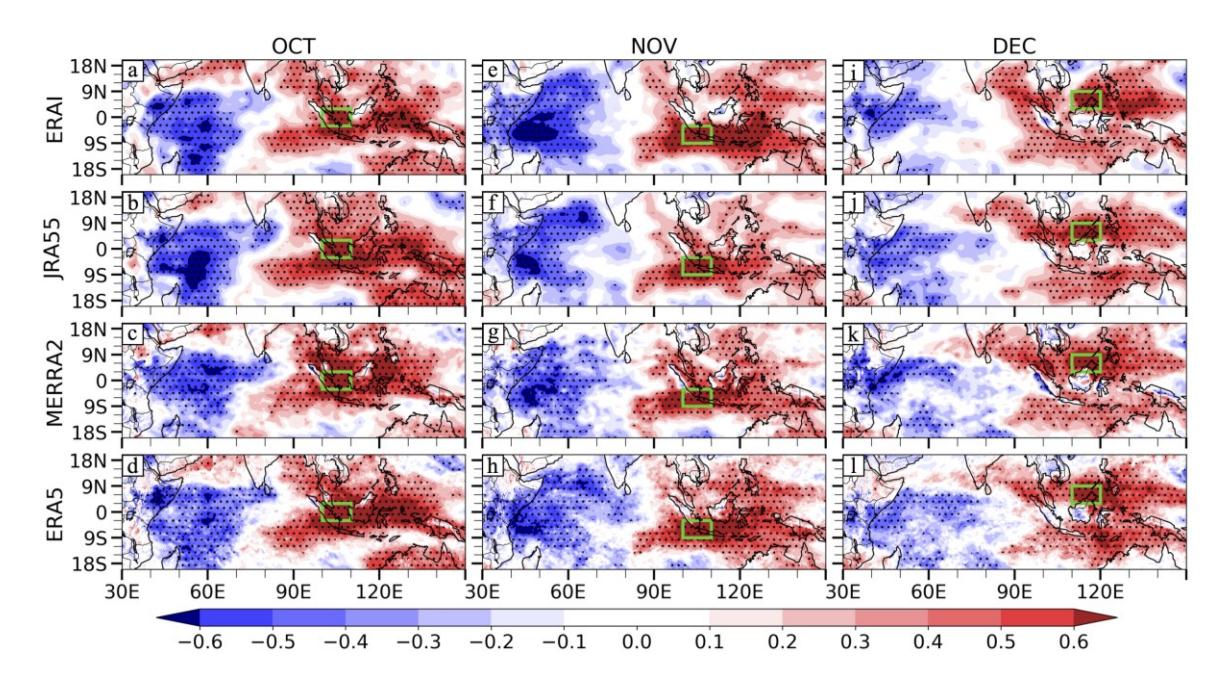
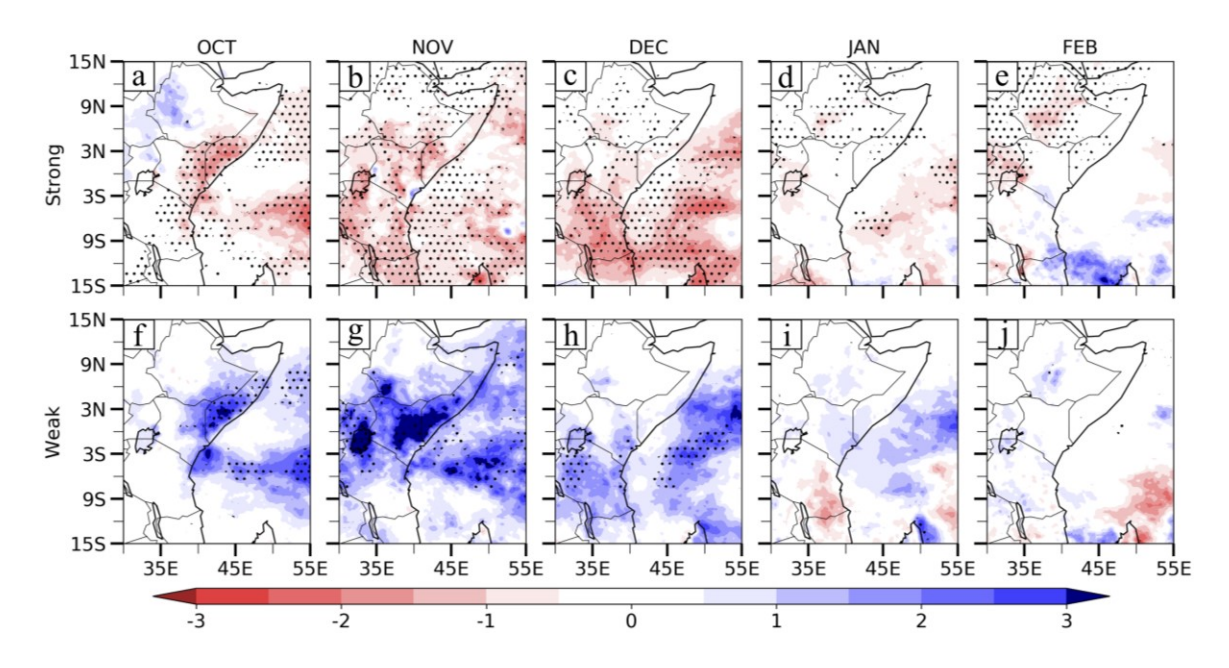


Figure 7. Correlations between  $\omega 500$  averaged over the Congo Basin (3°S – 3°N, 20 – 30°E) and  $\omega 500$  in ERAI in (a) June, (b) July, (c) August, and (d) September. (e) – (h), (i) – (l) and (m) – (p) are the same as (a) – (d), but for MERRA2, JRA55 and ERA5, respectively. Correlation coefficients exceeding the 95% confidence level are stippled, based on a two-tailed Student's t-test assuming 38 degrees of freedom (37 degrees of freedom for MERRA2).



**Figure 8.** Correlations between  $ω500IO_{32}$  (green boxes; 3°S - 3°N, 100 - 110°E) and ω500 in October for (a) ERAI, (b) JRA55, (c) MERRA2 and (d) ERA5. Correlations between  $ω500IO_{42}$  (green boxes; 3°S - 9°S, 100 - 110°E) and ω500 in November for (e) ERAI, (f) JRA55, (g) MERRA2 and (h) ERA5. Correlations between  $ω500IO_{23}$  (green boxes; 3°N - 9°N, 110 - 120°E) in December for (i) ERAI, (j) JRA55, (k) MERRA2 and (l) ERA5. Correlation coefficients exceeding the 95% confidence level based on a two-tailed Student's t-test assuming 38 degrees of freedom (37 degrees of freedom for MERRA2) are stippled.



**Figure 9.** Precipitation anomalies (mm·day<sup>-1</sup>) for the strong and weak composites in October – February in PERSIANN. Values exceeding 95% confidence levels are stippled, based on a Welch's t-test.

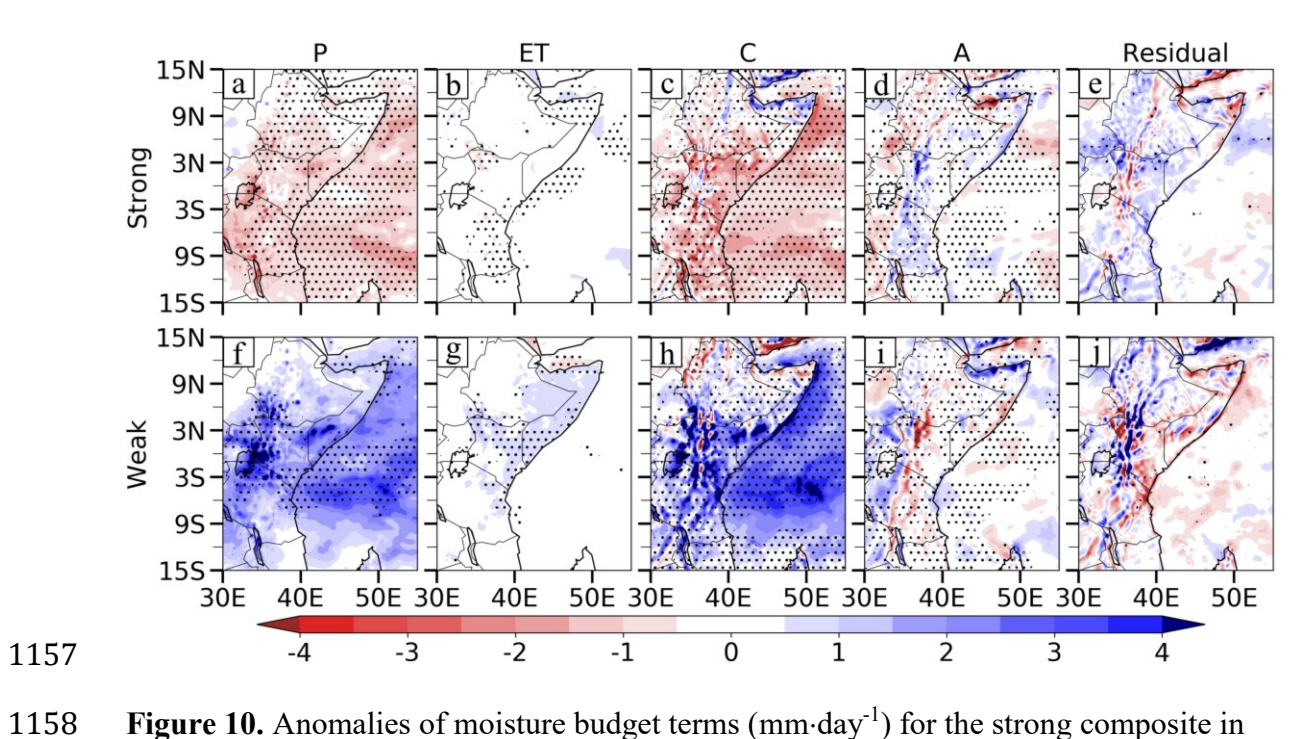


**Figure 10.** Anomalies of moisture budget terms (mm·day<sup>-1</sup>) for the strong composite in November calculated from ERA5: (a) P; (b) ET; (c) the C term; (d) the A term; and (e) the residual. (f) - (j) are anomalies of the moisture budget terms for the weak composite. Values exceeding the 95% confidence levels are stippled, based on a Welch's t-test.

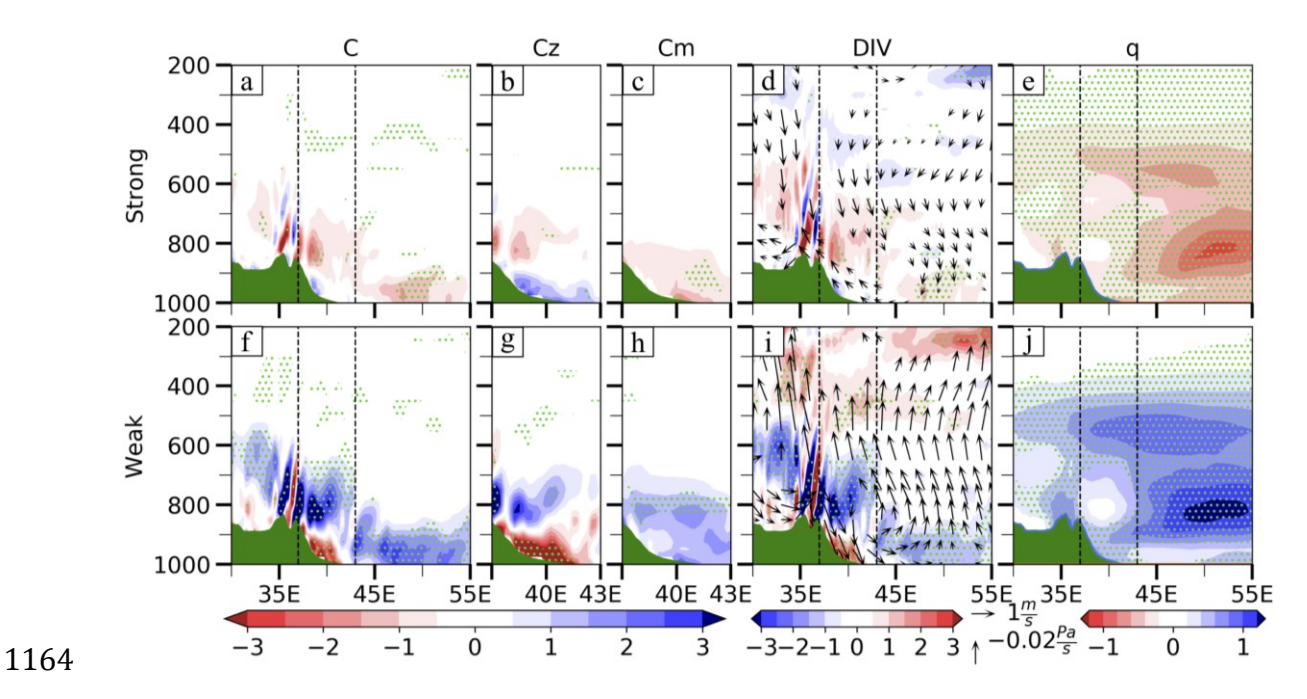


**Figure 11.** Cross sections of the anomalous (a) C term (C;  $10^{-8} \cdot \text{s}^{-1}$ ), (b) zonal component (Cz;  $10^{-8} \cdot \text{s}^{-1}$ ), (c) meridional component (Cm;  $10^{-8} \cdot \text{s}^{-1}$ ), (d) divergence (DIV;  $10^{-6} \cdot \text{s}^{-1}$ ),  $\omega$  (vectors;  $\text{Pa} \cdot \text{s}^{-1}$ ) and  $u_D$  (vectors;  $\text{m} \cdot \text{s}^{-1}$ ), and (e) specific humidity (q;  $10^{-3} \cdot \text{kg} \cdot \text{kg}^{-1}$ ) for the strong composite in November in ERA5, averaged between 3°S and 3°N. (f) – (j) are anomalies for the weak composite. For clarity, vectors exceeding the 95% confidence levels are plotted every 1.5° longitude and every other pressure level. Values exceeding the 95% confidence levels are stippled, based on a Welch's t-test. The dashed lines mark 37°E and 43°E. The green block represents the topography, constructed from climatological surface pressure (hPa) in ERA5.

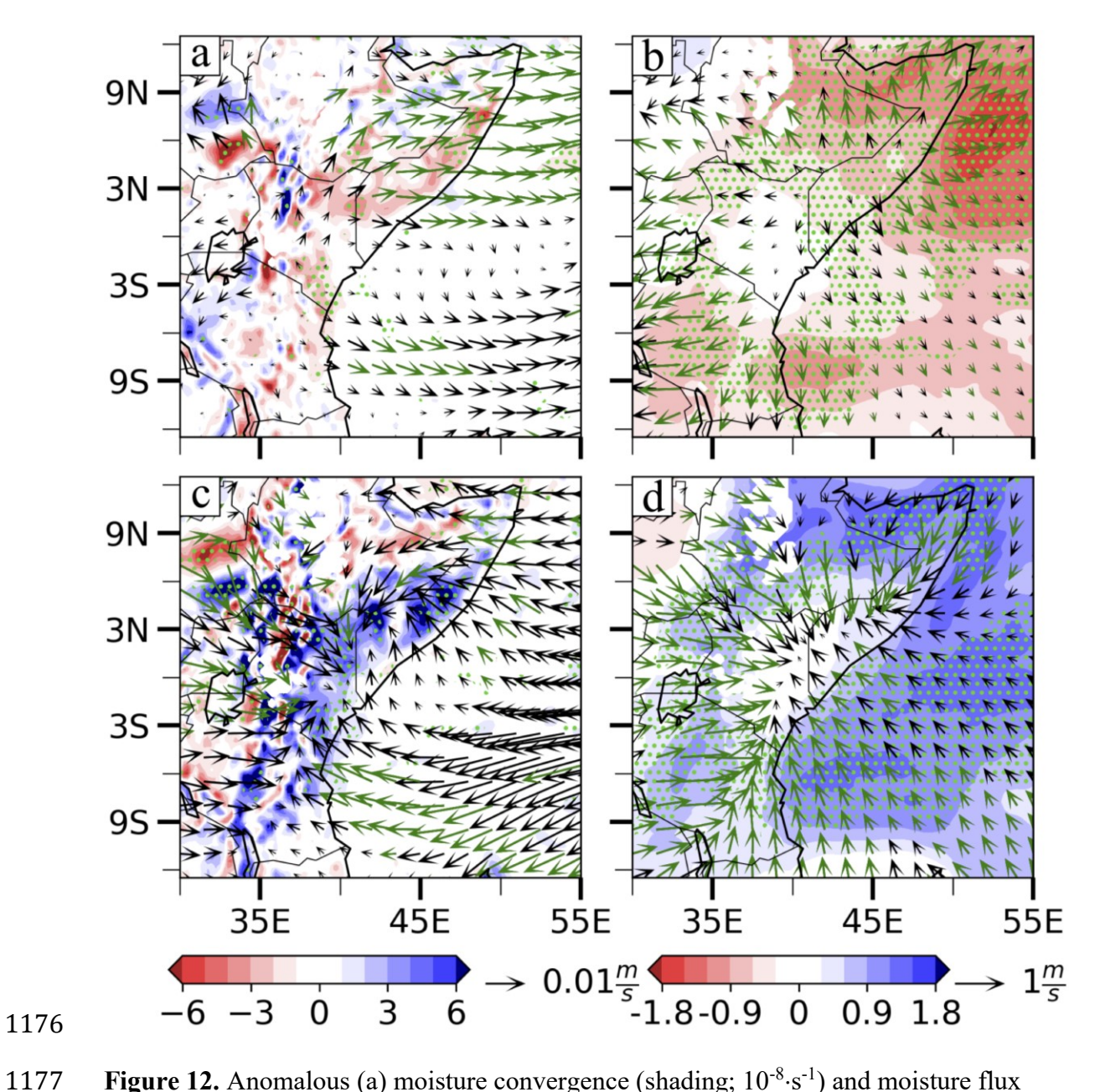


**Figure 12.** Anomalous (a) moisture convergence (shading;  $10^{-8} \cdot s^{-1}$ ) and moisture flux (vectors;  $m \cdot s^{-1}$ ), and (b) specific humidity (shading;  $10^{-3} \cdot kg \cdot kg^{-1}$ ) and divergent wind (vectors;  $m \cdot s^{-1}$ ) at 800 hPa for the strong composite in November in ERA5. (c) – (d) are anomalies for the weak composite. Vectors are plotted every 1.5° longitude/latitude for clarity, and marked green if exceeding 95% confidence levels. Values exceeding 95% confidence levels are stippled, based on a Welch's t-test.

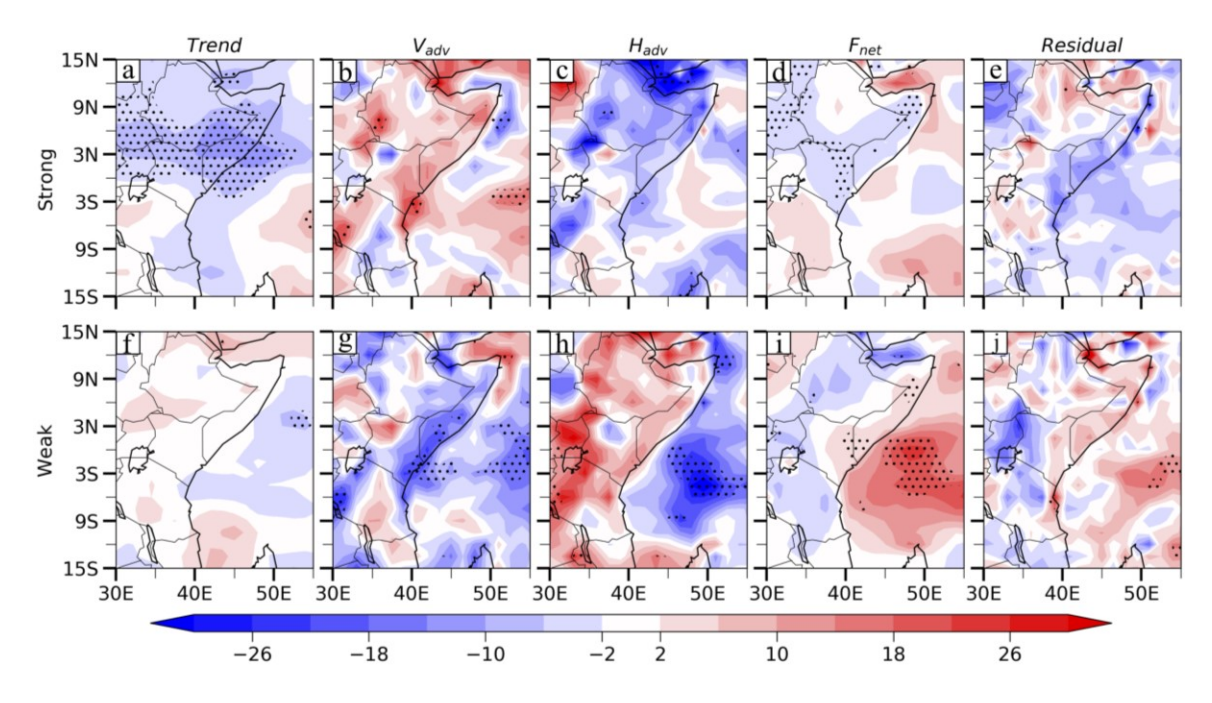


**Figure 13.** Anomalies of column-integrated MSE budget terms (W·m<sup>-2</sup>) for the strong composite in November calculated from 6-hourly data in ERAI: (a) the trend (b)  $V_{adv}$ , (c)  $H_{adv}$ , (d)  $F_{net}$ , and (e) the residual. (f) – (j) are anomalies of column-integrated MSE budget terms for the weak composite. Values exceeding the 95% confidence levels are stippled, based on a Welch's t-test.

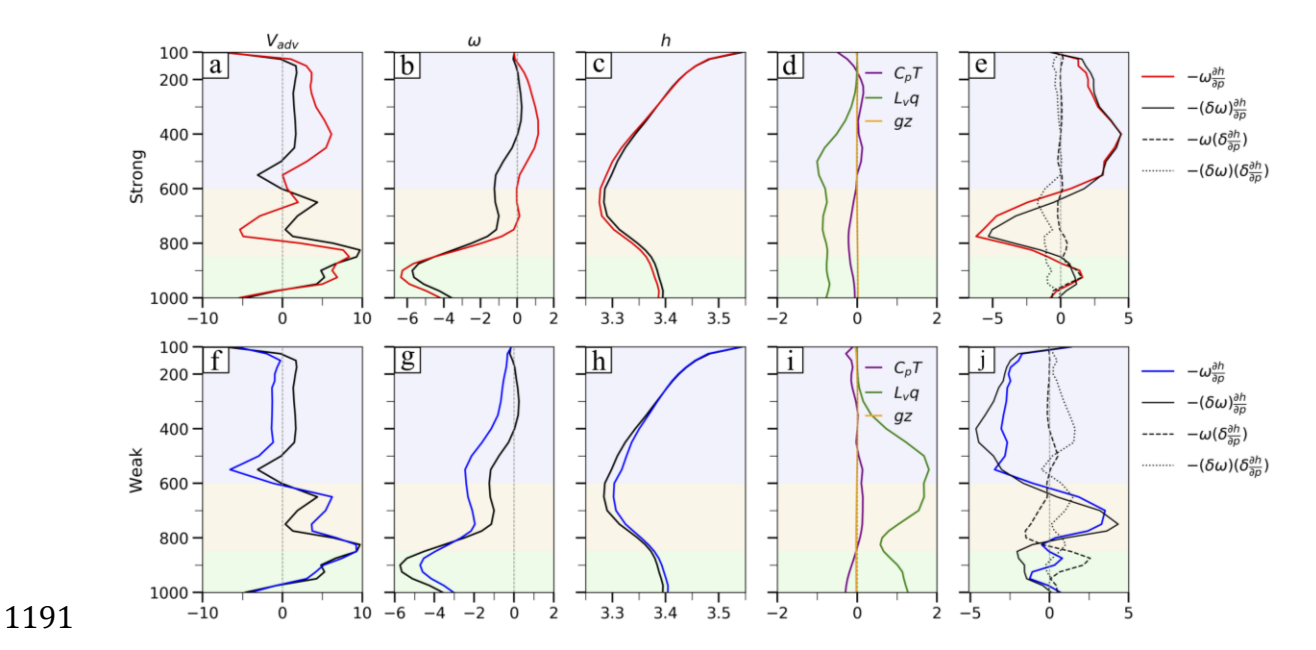


**Figure 14.** Vertical profiles of (a)  $V_{adv}$  ( $10^{-3} \cdot \text{W} \cdot \text{kg}^{-1}$ ), (b)  $\omega$  ( $10^{-2} \cdot \text{Pa} \cdot \text{s}^{-1}$ ), (c) MSE ( $10^{5} \cdot \text{J} \cdot \text{kg}^{-1}$ ), (d) anomalous MSE terms ( $10^{3} \cdot \text{J} \cdot \text{kg}^{-1}$ ) and (e) anomalous  $V_{adv}$  terms ( $10^{-3} \cdot \text{W} \cdot \text{kg}^{-1}$ ) for the strong composite (red lines) in November over the equatorial East Africa averaging region (Fig. 2), calculated from ERAI. (f) – (j) are diagnostics for the weak composite (blue lines). Black lines in (a) – (c) and (f) – (h) denote vertical profiles for the climatology.

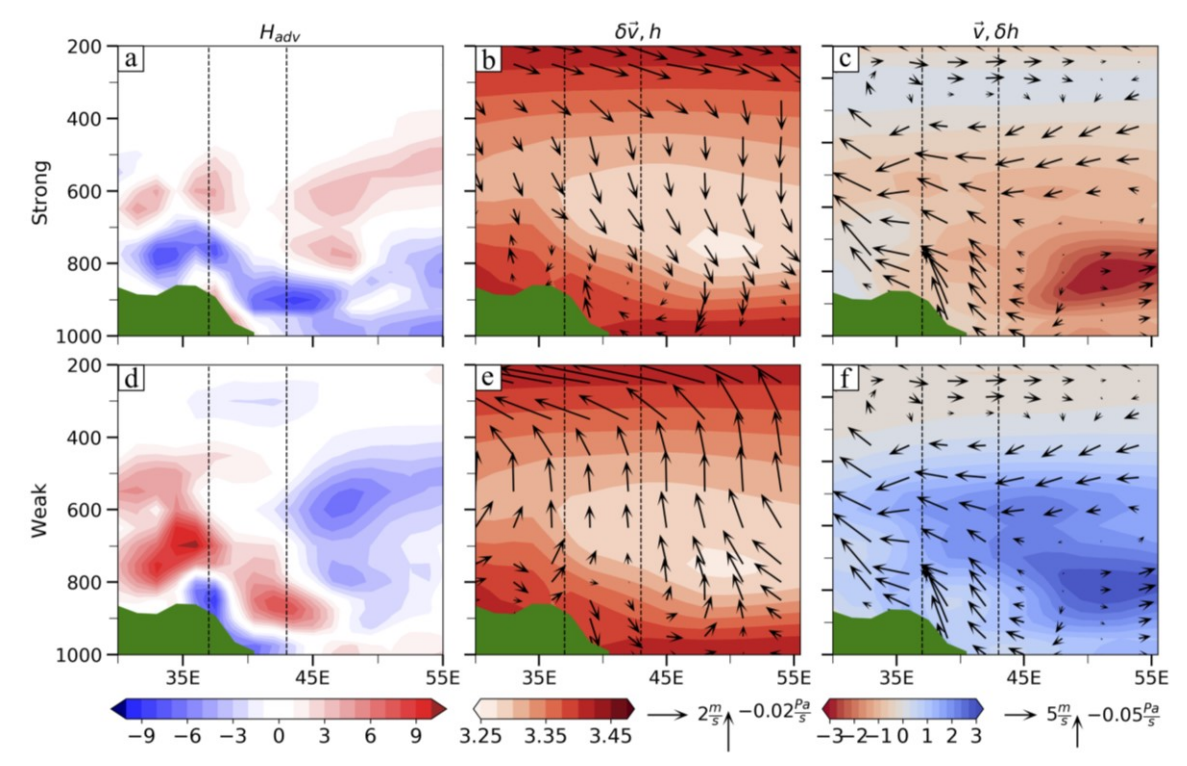


**Figure 15.** Cross sections of (a) the anomalous  $H_{adv}$  ( $10^{-3} \cdot \text{W} \cdot \text{kg}^{-1}$ ), (b) the climatological MSE ( $10^{5} \cdot \text{J} \cdot \text{kg}^{-1}$ ) and the anomalous zonal wind ( $\text{m} \cdot \text{s}^{-1}$ ) and vertical p-velocity ( $\text{Pa} \cdot \text{s}^{-1}$ ) and (c) the anomalous MSE ( $10^{3} \cdot \text{J} \cdot \text{kg}^{-1}$ ) and the climatological zonal wind ( $\text{m} \cdot \text{s}^{-1}$ ) and vertical p-velocity ( $\text{Pa} \cdot \text{s}^{-1}$ ) for the strong composite in November calculated from ERAI. (d) – (f) are diagnostics for the weak composite. Vectors are plotted every other longitude and pressure level for clarity. The green block represents the topography, constructed from climatological surface pressure (hPa) in ERAI.